Kitoga et al. (2026)
History and geochemical signatures of hydrothermally silicified volcanic and sedimentary rocks from the Paleoarchean (3.5–3.2 Ga) Barberton Greenstone Belt
Advances in Geochemistry and Cosmochemistry 2(1): 773, 10.33063/agc.v2i1.773

Research article

History and geochemical signatures of hydrothermally silicified volcanic and sedimentary rocks from the Paleoarchean (3.5–3.2 Ga) Barberton Greenstone Belt

Lungele Steve Kitoga[1,2]✉ Jean-François Moyen[1,3] Maud Boyet[1] Johanna Marin-Carbonne[4] Nicolas Olivier[1] Marion Garçon[1] Gary Stevens[2]

[1] Laboratoire Magmas et Volcans, Université Clermont Auvergne, CNRS, IRD, OPGC, F-63000 Clermont-Ferrand, France
[2] Department of Earth Sciences, University of Stellenbosch, Private Bag X1, Matieland 7602, South Africa
[3] Département de Géologie, Université Jean Monnet, Saint-Etienne 42023, France
[4] Institut des Sciences de la Terre, Université de Lausanne, 1015 Lausanne, Switzerland

✉ **Correspondence to:** Lungele Steve Kitoga: kitogastevel@gmail.com

Author contributions: Conceptualization: KLS, MJF, BM, MCJ, ON; Formal analysis: KLS, BM, MCJ; Investigation: KLS, MJF, BM, MCJ; Writing — Original Draft: KLS; Writing — Review & Editing: KLS, MJF, BM, MCJ, ON, GM, SG; Supervision: MJF, BM, MCJ, SG; Funding acquisition: MJF, BM, SG; Validation: BM, ON, GM, SG

Data, code, and outputs: https://doi.org/10.25519/QXR1-9Y88

Submitted: 2025-05-20
Accepted: 2026-01-20
Published: 2026-02-23

Production editor:
James Darling

Handling editor:
Ramananda Chakrabarti

Reviews:
Alex McCoy-West
and one anonymous reviewer

Copyediting:
Yingbo Li,
Anselm Loges,
Marthe Klöcking

Seafloor-derived silicified volcanic and sedimentary rocks provide unique records of hydrothermal systems that operated at the top of the Paleoarchean submerged crust. Based on petrographic, thermometric, and geochemical analyses, we distinguish the signatures of Paleoarchean hydrothermal activity from those due to subsequent metamorphism and weathering in silicified volcanic and sedimentary rocks sampled from the 3.5–3.2 Ga Barberton Greenstone Belt. Measured ^{138}La-^{138}Ce and ^{147}Sm-^{143}Nd isotopic compositions indicate that weathering by post-Archean oxidised fluids modified LREE abundances in samples displaying Ce anomalies. Raman spectroscopy of carbonaceous material, chlorite thermometry and oxygen isotope thermometry provide evidence for mineralogical resetting by regional metamorphism at $\sim 350 \pm 50$ °C, which arguably did not modify the bulk-rock geochemistry. Oxygen isotope fractionation in a quartz-carbonate assemblage preserved from subsequent resetting provides a minimum temperature of $\sim 110 \pm 50$ °C interpreted as the highest possible temperature of the Paleoarchean silicifying hydrothermal fluids. Y/Ho and Zr/Hf ratios are chondritic in silicified volcanic and clastic sedimentary rocks, which differentiates them from Archean orthochemical cherts with suprachondritic Y/Ho and Zr/Hf ratios. Finally, silicified volcanic rocks that are free of Ce anomalies (mostly unweathered by oxidising fluids) display slightly lower Sm/Nd ratios and more variable Lu/Hf ratios than non-silicified counterparts, which we ascribe to differential REE mobilisation by silicifying hydrothermal fluids. The modification of Sm/Nd and Lu/Hf ratios during Paleoarchean hydrothermal activity should be integrated in future Sm-Nd and Lu-Hf isotopic investigations of hydrothermal inputs to Archean ocean chemistry and of recycled seafloor-derived rocks.

1 Introduction

Silica-rich supracrustal rocks from the Paleoarchean (3.6–3.1 Ga) constitute some of the oldest preserved records of Earth's surface and oceanic environments. These rocks are of particular interest as they offer insights into ocean composition, hydrothermal fluid properties, and crustal processes on the early Earth. These lithologies can broadly be divided into two categories. The first group includes chemical sedimentary rocks, such as cherts and banded iron formations (BIF), which precipitated directly from seawater. Their composition suggests that early oceans were near saturation with respect to silica (André et al., 2022; Robert and Chaussidon, 2006; Siever, 1992), but also contained high concentrations of dissolved ferrous iron, as a result of anoxic conditions prevailing at that time (Konhauser et al., 2017; Planavsky et al., 2011). These chemical sedimentary rocks are thus considered key archives of the physico-chemical properties of Paleoarchean seawater (Jaffrés et al., 2007; Kasting et al., 2006; Lowe et al., 2020).

The second category of silica-rich supracrustal rocks consists of hydrothermally silicified volcanic and clastic sedimentary units that formed beneath ancient oceans through the replacement of primary magmatic and detrital phases by silica, due to the circulation of seawater-derived, silica-rich hydrothermal fluids (Abraham et al., 2011; André et al., 2022; Brengman and Fedo, 2018; de Wit and Furnes, 2016; Hofmann and Wilson, 2007; Paris et al., 1985). This observation raises concerns that at least some chemical sedimentary rocks, regarded as direct archives of early ocean chemistry, underwent similar fluid-rock interaction processes on the seafloor, which could overprint their original record (Kitoga et al., 2024). Moreover, most Paleoarchean terrains have been subjected to regional metamorphism, which can range from simple recrystallisation, preserving bulk-rock geochemistry (Condie et al., 1977; Lécuyer et al., 1994), to more intense overprinting involving elemental remobilisation at the whole-rock scale (Hayashi et al., 2004; Weis and Wasserburg, 1987a). Evaluating the effects of metamorphism on mineralogical and geochemical proxies, such as chlorite chemistry, Raman spectra of carbonaceous material and $\delta^{18}O$ values in quartz and carbonates, (e.g. Heck et al., 2011; Johnson and Wing, 2020), is therefore crucial for avoiding biases in the reconstruction of Paleoarchean fluid temperatures and conditions. In addition to hydrothermal and metamorphic overprinting, many silica-rich Paleoarchean rock exposures have interacted with surface meteoric waters (Lowe and Byerly, 2007b; Reimann et al., 2021; Saitoh et al., 2021), further modifying their geochemical signatures. Such weathering processes have been shown to affect rare earth element (REE) patterns (Banerjee et al., 2016; Bonnand et al., 2020; Planavsky et al., 2020; Pfennig et al., 2025). As a result, there is an ongoing debate regarding the use of certain elemental ratios, such as Zr/Hf and Y/Ho, to distinguish seawater-precipitated sediments from hydrothermally silicified volcanic rocks (Bolhar et al., 2004; Brengman and Fedo, 2018; Yoshida et al., 2024). Combining petrography, elemental concentration, isotope systematics, and thermometric proxies can help distinguish preserved primary signatures from those overprinted by secondary events in silicified rocks derived from the Archean seafloor.

This study investigates the mineralogical and geochemical composition of silicified volcanic rocks and clastic sedimentary rocks from the 3.5–3.1 Ga Barberton Granitoid-Greenstone Terrain. The samples analysed were collected from five stratigraphic sections comprising volcanic units and sedimentary units, spanning in age from 3.53 to 3.3 Ga. In addition to previously published mineralogical and geochemical data on silica-rich rocks from the Onverwacht Group (Abraham et al., 2011; Duchac and Hanor, 1987; Geilert et al., 2014; Grosch, 2018; Hanor and Duchač, 1990; Hofmann et al., 2013; Hofmann and Harris, 2008; Kitoga et al., 2024; Ledevin et al., 2019, 2014, 2015; Marin-Carbonne et al., 2011; Rouchon and Orberger, 2008; Stefurak et al., 2015; Tice et al., 2004; Xie et al., 1997; Zakharov et al., 2021), new petrographic observations, thermometric data (including Raman spectroscopy of carbonaceous material, chlorite thermometry, in-situ oxygen isotope thermometry in quartz-carbonate assemblages), and bulk-rock geochemical measurements (major and trace elements, La-Ce and Sm-Nd isotopic systematics) on silicified volcanic and sedimentary rocks are presented. The objectives of this study are (1) to assess the potential overprints of metamorphism and weathering on the mineralogy and geochemistry of the analysed rocks, thereby offering a critical evaluation of the compositional evolution of the rocks throughout their history; (2) to quantify the temperature of Paleoarchean silica-rich hydrothermal fluids; and (3) to pinpoint the specific geochemical signatures resulting from the circulation of hydrothermal fluids in the Paleoarchean supracrustal rocks.

2 Geological setting and samples

2.1 Regional geology

The 3.5–3.1 Ga Barberton Granitoid-Greenstone Terrain is located in the NE part of the Kaapvaal Craton in Southern Africa. It comprises four different generations of granitoids surrounding a succession of supracrustal rocks known as the Barberton Greenstone Belt (Figure 1; Moyen et al., 2019; Byerly et al., 2019). The investigated Onverwacht Group is the lowermost stratigraphic subdivision of the Barberton Greenstone Belt and largely consists of mafic to ultramafic volcanics that emplaced in a sub-oceanic setting (Armstrong et al., 1990; Byerly et al., 2019; Lowe and Byerly, 1999). It is overlain by large sedimentary successions belonging to the 3.3–3.2 Ga Fig Tree and Moodies groups (Figure 1; Drabon and Lowe, 2021; Heubeck, 2019; Heubeck and Lowe, 1994). Some lava flows of the Onverwacht Group are silicified at their tops due to the circulation of seawater-derived hydrothermal fluids and overlain by sedimentary layers (Hofmann et al., 2013; Hofmann and Harris, 2008; Paris et al., 1985). These sedimentary layers are largely dominated by variably silicified clastic sedimentary rocks, commonly identified as cherts sensu lato when their SiO_2 content exceeds ~80 wt %, although some detritus-free orthochemical cherts (or cherts sensu stricto) are also locally present (Knauth and Lowe, 1978; Ledevin et al., 2019; van den Boorn et al., 2010). Cherts are generally classified on the basis of their macroscopic appearance as grey, black and black-and-white chert (Hofmann et al., 2013; Lanier and Lowe, 1982; Ledevin et al., 2014), although the correlation between this classification and chert's origin remains unclear. Occasionally, non-silicified sedimentary rocks are also preserved within the Onverwacht Group (Dziggel et al., 2002; Lowe and Byerly, 2020).

A major geodynamic event deformed and metamorphosed the Onverwacht Group ~3.2 Ga ago. The age of this tectono-metamorphic event was determined by dating garnet, monazite and titanite from lower Onverwacht Group rocks in the southern part of the belt which was subjected to high-pressure amphibolite facies conditions of ~7.5 kbar and 550 °C (Cutts et al., 2015; Diener et al., 2005). Despite folding, the portion of the Onverwacht Group that occurs

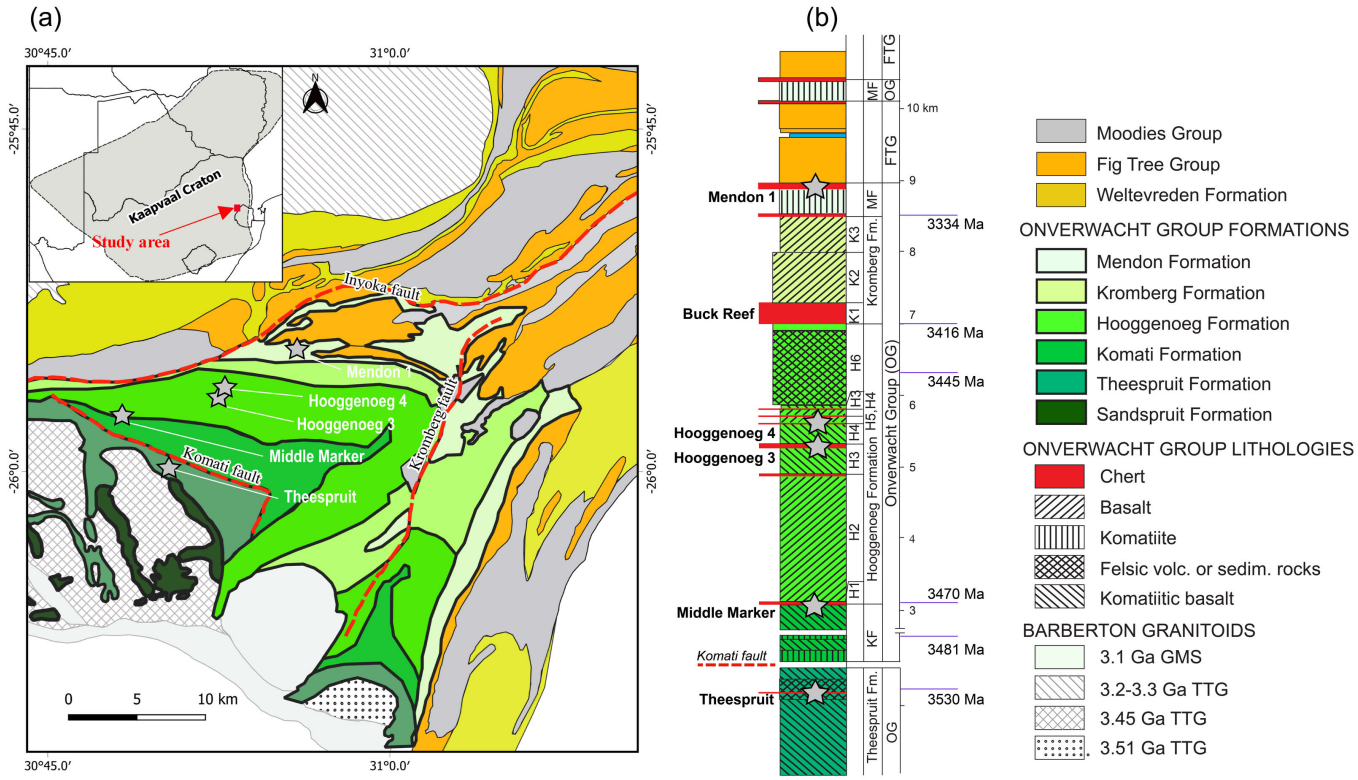

Figure 1. (a) Simplified geological map of the Barberton Granitoid-Greenstone Terrain and (b) Stratigraphic succession of the central part of the Barberton Greenstone Belt modified after Anhaeusser (1981) and Hofmann and Harris (2008). Grey stars indicate the positions of the studied sections on the map and on the stratigraphic succession.

above the Komati Fault is generally agreed to represent a > 9 km-thick continuous and seafloor-deposited volcano-sedimentary succession (Hofmann and Harris, 2008; Lowe and Byerly, 2007a). This succession includes four different stratigraphic units: Komati, Hooggenoeg, Kromberg and Mendon formations (Figure 1; see recent review by Byerly et al., 2019). The Sandspruit and Theespruit formations, located below the Komati Fault, were buried to depths of at least 25 km during the ~3.2 Ga amphibolite facies event, and represent a much deeper crustal section that was exhumed along the Komati Fault at 3.2 Ga (Kisters et al., 2003; Stevens and Moyen, 2007). Despite these structural complexities, the geological formations constituting the Onverwacht Group collectively comprise distinguishable stratigraphic members, each of which represents one or several layers of volcanic material (generally silicified at the top) and overlying sedimentary units (Byerly et al., 2019; Hofmann and Harris, 2008).

2.2 Studied sections and samples

Studied samples originated from five different stratigraphic sections (Figure 2) that include sedimentary layers (comprising black cherts, grey cherts, black-and-white cherts or schistose felsic sediments) and silicified volcanic rocks. The lithologies featured in Figure 2 are based on lithological descriptions at outcrop scale and petrographic descriptions at hand-specimen and thin-section scales, and each section is named after the stratigraphic unit to which it belongs. Drone images of the studied sections with exact sample location are provided as Supporting Figures (S1-S4; Kitoga et al., 2025).

2.2.1 *The Theespruit section*

The Theespruit section was previously described by Hofmann and Harris (2008) and is part of the amphibolite facies portion of the Onverwacht Group. The felsic rocks of the Theespruit section were dated at ~3.53 Ga by Kröner et al. (2016). It is exposed in a river bed within the Tjakastad locality that was previously studied for lithological and mineralogical compositions by Diener et al. (2005) and Hofmann and Harris (2008). From the base upward, this section consists of amphibolitic pillows and amphibolite schists (> 30 m) representing metamorphosed volcanic rocks, overlain by a black chert layer (< 1 m) and felsic metasedimentary schists (~14 m; Figure 2a). Representative samples for each of these lithological types were considered in this study.

2.2.2 *The Middle Marker section*

The Middle Marker section comprises ~3.48 Ga old cherts and silicified volcanic rocks situated at the top of the Komati Formation (Figures 1, 2b). Our Middle Marker samples were collected from a ~7 m thick portion of a chert unit and from more than 30 m of the underlying silicified volcanic rocks (Figure 2b). A relatively fresh volcanic rock sample (SK-KM02) was also obtained downwards of the stratigraphic succession, more than 100 m below the interface between sedimentary and volcanic rocks. The cherts were interpreted by Lanier and Lowe (1982) to represent silicified volcaniclas-

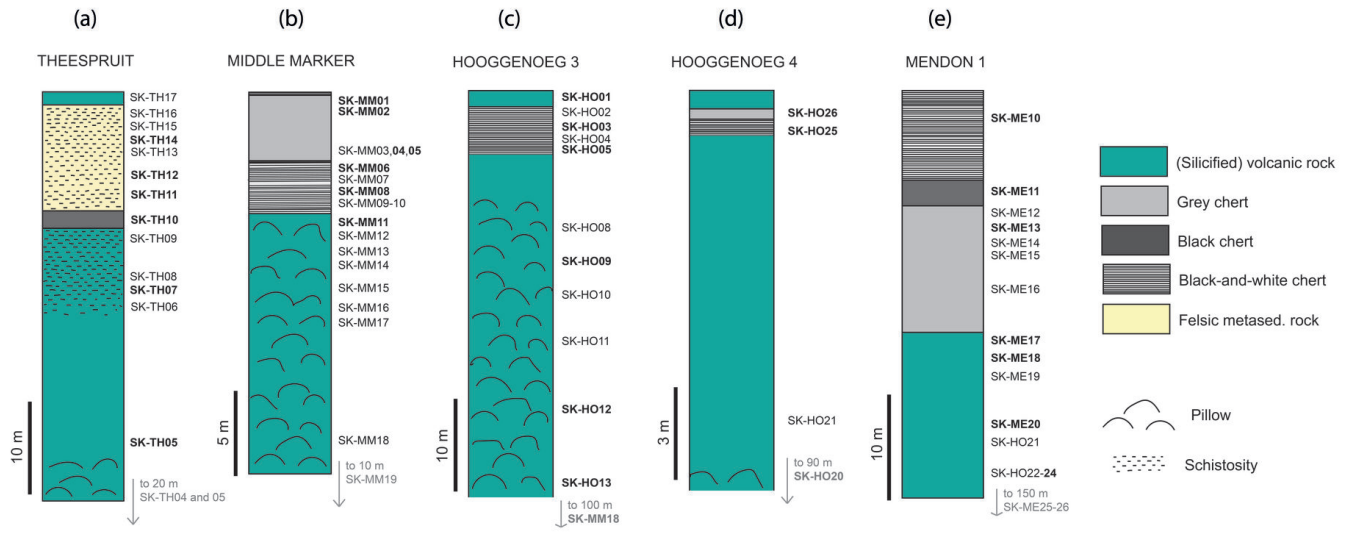

Figure 2. Detailed lithostratigraphic logs of the studied localities with the location of collected samples: (a) Theespruit section, (b) Middle Marker section, (c) Hooggenoeg 3 section, (d) Hooggenoeg 4 section, (e) Mendon 1 section. The location of each stratigraphic section on the geological map and stratigraphic succession of the Barberton Greenstone Belt is shown in Figure 1. In bold are samples that were selected for major and trace element, isotopic and thermometric analyses.

tic components that were initially deposited in a relatively shallow sub-aqueous environment. These sedimentary rocks currently occur as grey, black, and black-and-white cherts that preserve primary sedimentary structures, confirming a clastic origin; a representative sample was considered for each of these lithological types (Figure 2b).

2.2.3 The Hooggenoeg 3 and 4 sections

The Hooggenoeg 3 and 4 sections formed between the 3.48 Ga age of Komati Formation and the 3.41 Ga age of felsic volcanic rocks from the Buck Reef Unit (Figure 1; Armstrong et al., 1990). The Hooggenoeg 3 section is made of > 100 m-thick silicified and ocelli-bearing pillows together with overlying ~ 6 m-thick black-and-white cherts (Figure 2c; Hofmann and Harris, 2008). The Hooggenoeg 4 section includes a ~ 1 m thick chert layer comprising grey and black-and-white chert layers as well as a silicified basaltic unit exceeding 100 m in thickness (Figure 2d). Unfortunately, the upper 5–8 m of the topmost volcanic rocks underlying both Hooggenoeg 3 and Hooggenoeg 4 cherts showed macroscopic evidence of intense surface weathering mostly transforming them into soil and could therefore not be sampled for the present study.

2.2.4 The Mendon 1 section

The Mendon 1 section (also called Msauli or Umsoli section in the literature; e.g. Heinrichs, 1984; Lowe and Byerly, 1986; Rouchon and Orberger, 2008) is named after the Mendon 1 Chert Unit situated at its top. The sedimentary portion of this section is slightly over 20 m-thick and comprises black-and-white, black and grey cherts that were previously interpreted to represent silicified volcaniclastic sedimentary rocks (Figure 2e; Heinrichs, 1984; Rouchon and Orberger, 2008; Stanistreet et al., 1981; Trower and Lowe, 2016). The deposition of these cherts was estimated to have occurred around 3.33 Ga based on zircon U-Pb geochronology (Decker et al., 2015). These cherts are underlain by silicified volcanic units displaying various textures that include the hydrothermally induced zebraic texture as well as relicts of the magmatic spinifex texture (Hanor and Duchač, 1990; Hofmann and Harris, 2008). We sampled each chert unit together with the top 15 m of silicified volcanic effusive rocks occurring directly below the Mendon 1 chert layer for this study (Figure 2e). In addition, relatively fresh volcanic rocks (SK-ME26 and SK-ME27) were also sampled more than 150 m below the Mendon 1 chert.

3 Methods

After lithological description of the outcrops, representative samples were collected from each of the five studied sections. The samples were collected from surface outcrops using a hammer and a chisel. Each sample was cut into cm-thick rock slabs of which different slabs per sample were dedicated to thin section and powder preparation. With the prepared thin sections, petrographic studies were performed using a polarising microscope and a Zeiss EVO MA15 scanning electron microscope (SEM) coupled with an Oxford INCA energy-dispersive spectrometer at Stellenbosch University. Backscattered electron images were acquired at a working distance of ~ 8.5 mm, an accelerating voltage of 20 kV and a measurement current of ~ 19.5 nA. Additionally, a tungsten-carbide jaw crusher and an agate ball mill were used for rock powder preparation. During powder preparation, an effort to remove as much weathered surface as possible was made.

3.1 Raman spectrometry and the carbonaceous material thermometer

We acquired 45 Raman spectra of carbonaceous materials from four different chert samples: SK-MM06 from the Komati section, SK-HO03 from Hooggenoeg 3, SK-HO25 from Hooggenoeg 4 and SK-ME11 from the Mendon 1 section. These analyses were performed using an InVia confocal Raman micro-spectrometer equipped with a 532 nm diode laser, a Peltier-cooled CCD detector of 1024 x 256 pixels, an automatised stage and a Leica DM 2500M optical microscope at Laboratoire Magmas et Volcans, University Clermont Auvergne. Before analytical sessions, the spectrometer was calibrated to a reference Si peak at $520.5 \pm 0.5\ cm^{-1}$. Analyses were carried out on ~30 µm-thick polished thin sections and targeted carbonaceous materials that were covered by 4–6 µm of quartz to avoid detecting deteriorations due to polishing. Acquisition time was calibrated at 6 times 15 s for each point. During acquisition, the laser beam passed through a 100× microscope objective under standard confocality (slit aperture set to 65 µm) with a final power of 1 to 4 mW at the analysed surface. Spatial resolutions of 1 to 3 µm and a spectral resolution better than $1\ cm^{-1}$ were achieved. We used Wire 4.2 software to perform the following actions of data treatment: (1) correct for fluorescence effects by applying a linear baseline, (2) crop only the 1100–1850 cm^{-1} from the original spectra (acquired between 500 and 2400 cm^{-1}), (3) deconvolute and fit the different curves corresponding to carbonaceous material peaks by a series of iterative calculations, and finally (4) measure the areas occupied by each peak.

The equilibrium temperature of carbonaceous materials is routinely estimated based on the release of heteroatoms and hydrogen, associated with a reorganisation of carbonaceous materials into crystalline graphite with increasing temperature (Beyssac et al., 2002). At low temperature (100 to 600 °C), the Raman spectra of carbonaceous materials display the G peak of graphite at a shift of ~1580 cm^{-1} and four D peaks representing disorganised carbon that occur respectively at ~1350 cm^{-1} (D1), ~1610 cm^{-1} (D2), ~1450 cm^{-1} (D3) and ~1190 cm^{-1} (D4). Progressive reductions of D peaks and enhancement of the G peak during the elevation of the temperature allowed Beyssac et al. (2002) to propose a thermometer that is applicable to samples that equilibrated at peak temperatures of 300 to 600 °C. This calibration is expressed as follows: T (°C) = -445×R2+641, where R2 is given by R2 = D1/(D1+D2+G), and spectral values (i.e. D1, D2 and G) are considered as integrated areas for the respective peaks (Beyssac et al., 2002).

3.2 Secondary ion mass spectroscopy (SIMS)

The CAMECA 1280 HR SwissSIMS instrument was used for oxygen isotope analyses on quartz and carbonate phases at the University of Lausanne. These analyses were conducted on 3 x 4 cm portions of thin sections that were pressed into indium mounts together with quartz and carbonate standards. The topography of the indium mounts did not exceed 5 microns of elevation difference, as determined with a Bruker GT-K white light interferometer. Three quartz-carbonate couples from SK-ME18 (Mendon 1 section) and one couple from SK-MM11 sample (Komati section) were selected for SIMS analyses of 4 to 7 carbonate spots and 7 to 11 quartz spots. At 10 kV, a 1.3 nA primary beam of Cs^+ ions was focused to a 15-micron-sized spot diameter. The mass resolving power was set at 2400 using an entrance slit of 122 microns and multicollection exit slits of 1 to resolve mass interferences due to the OH^- contribution. O isotopes were measured in multicollection mode, on two off axis Faraday cups. Each analysis lasted ~3 minutes that included 30 s of pre-sputtering, allowing centering of the secondary beam and background measurements of Faraday cups, and 20 cycles of 5 seconds of secondary ions collection. The data initially obtained as $^{18}O/^{16}O$ ratios were converted into the classical delta-notation relative to VSMOW reference $[\delta^{18}O = 1000 \times [(^{18}O/^{16}O_{sample}) - (^{18}O/^{16}O_{VSMOW})] / (^{18}O/^{16}O_{VSMOW})]$. Repeated analyses of UNIL-Q1 reference quartz allowed correcting of quartz analyses for instrumental mass fractionation and provided an external error range (2 SD) of 0.4 ‰ for $\delta^{18}O$ analyses. Additionally, repeated analyses of the UNIL-C1 (2 SD = 0.5 ‰), UNIL-C4 (2 SD = 0.3 ‰) and KPIK (2 SD = 0.5 ‰; see Supporting Table S1; Kitoga et al., 2025) reference materials allowed correcting of carbonate analyses for instrumental mass fractionation considering effects of major element compositions (i.e. calcite versus ankerite; Bégué et al., 2019; Rollion-Bard and Marin-Carbonne, 2011; Śliwiński et al., 2018, details on these corrections can be found in Table S8).

3.3 Electron probe micro-analyses (EPMA)

Major and minor element compositions were measured for (1) all the carbonate grains analysed by SIMS, and (2) for chlorites found within areas exceeding 100 micrometre square in three sedimentary rock samples (SK-MM02, SK-MM05, SK-ME13) and one silicified volcanic rock sample (SK-ME24) using a CAMECA SX Five EPMA instrument at the University Clermont Auvergne. As required by the XMapTools software that was used to process these data (Lanari et al., 2014), we coupled X-ray maps of areas reaching 350 x 350 µm with qualitative analyses of specific zones within these areas. Qualitative analyses were performed with a current of 15 nA, an accelerating voltage of 15 kV and a counting time of 20 s. For acquisition of X-ray maps, a 100 nA current was applied with a dwell time of 0.1 s and a step size of 1 µm. The following internal standards were used for calibration during quantitative analyses: albite for Si, forsterite for Mg, fayalite for Fe, orthoclase for K and Al, anorthite for Ca, rhodonite for Mn and calcite for Ca.

3.4 Bulk-rock major and trace element analyses by XRF and ICPMS

Thirty-two representative samples were analysed for major and trace elements at Stellenbosch University and University Clermont Auvergne, respectively. The volatile content or loss on ignition (LOI) was calculated after keeping ~2 g of rock powders in a muffle furnace at 1000 °C for a duration

of 30 minutes. For analyses of the non-volatile major elements, homogeneous discs were prepared by mixing 0.5 g of powder with 5 g of flux (32.8 % $LiBO_2$ + 66.7 % $Li_2B_4O_7$ + 0.5 % LiI) and fusing the mixture at 1000 °C in an automatic Claisse M4 Gas Fusion instrument. A PANalytical Axios wavelength-dispersive X-ray fluorescence (XRF) spectrometer was used to quantify the major element concentrations at Stellenbosch University. Reference materials that are typically used for calibration of XRF analyses at Stellenbosch University include SARM, NIST and USGS geological standards. Several certified geological reference materials including three basalts (BE-N, JB-1, BHVO-1), one granodiorite (JG-1), and two granites (HUSG-1 and WITS-G) were analysed repeatedly along with the samples and returned a 2 SD value that was lower than 0.8 wt % for SiO_2 and Al_2O_3, and lower than 0.1 wt % for all the other major oxides. Deviation of analysed reference material compositions from published values is generally below ± 5 % (see Table S2).

Trace element concentrations were analysed using an Agilent Technologies 8900 QQQ-ICP-MS at Laboratoire Magmas et Volcans, University Clermont Auvergne. Approximately 50 mg of powder and 200 mg of crystalline NH_4HF_2 were weighed into Savillex beakers and kept for 24 hours at 220 °C in a furnace. After receiving 1 ml of 14 M HNO_3, the beakers were kept at 90 °C overnight and dried out on a hot plate. Three successive series of dissolution in 0.5 ml 14 M HNO_3 at 90 °C and drying on a hot plate allowed getting rid of residual fluorides. The samples were then completely dissolved in 30–40 ml of 7 M HNO_3 of which an aliquot corresponding to 2.5 % of the dissolved rock powder was taken for analysis. After complete evaporation, the aliquot was finally dissolved in a solution made of 0.4 M HNO_3 - 0.05 M HF and enriched to 2 ppb of Re, In and Bi that served for monitoring the stability of the signal during the sequences of analysis and for correcting the drift if necessary. We used a dilution factor of 5000. The counts per second measured in the solutions were converted to concentrations by bracketing our samples with repeated measurements of the USGS BHVO-2 certified standard. The signal of chemical blanks was insignificant but was still removed from unknowns to mitigate instrumental and chemistry-induced errors. Repeated analyses of certified geological reference materials including one granite (G2), four basalts (BIR-1a, BE-N, JB-3, JB-1), one serpentinite (UBN) and one banded iron formation (IFG) allowed estimating the repeatability and the accuracy of our measurements (see Table S3). Transition metals were measured using the collision cell (He mode) and all other elements in "no gas mode". Reference materials provided both 2 RSD and differences from previously published values that are lower than 5 % for elements of interest in this study, namely REEs, Y, Rb, Zr and Hf (Table S3).

3.5 Sm-Nd and La-Ce isotope analyses

Eleven samples were selected and processed along with the BHVO-2 reference material and one chemical blank for analyses of ^{138}La-^{138}Ce and ^{147}Sm-^{143}Nd isotopic systematics. These samples are representative of the different lithological types (i.e. silicified volcanic and sedimentary rocks) and were selected considering their chondrite-normalised REE patterns (e.g. variable Ce anomaly: Ce/Ce^*_{PAAS} = 0.39–1.39). Depending on the REE contents, 50 to 300 mg of rock powders were weighed into Savillex beakers, dissolved using 29 M HF - 14 M HNO_3 in proportion 3:1 and placed for 48 hours on a hot plate. Once evaporated, samples were dissolved (and dried) several times in concentrated HNO_3. Final solutions were prepared by dissolving dry contents of the beakers in 5 to 18 ml of 6 M HCl. Aliquots consisting of 94 %, 5 % and 1 % of the prepared solutions were separated and were respectively used for (1) the separation of Ce and Ce isotopic measurement; (2) measurement of the Sm-Nd systematics using the isotope dilution technique (^{149}Sm-^{150}Nd mixed spike); and (3) determination of the La/Ce ratios by ICPMS, respectively.

Cerium fractions were isolated in 3 steps previously described in detail by Israel et al. (2020). Briefly, the aliquots were firstly loaded in 2.5 M HCl into AG50W-X8 columns. Major elements were removed using 2.5 M HCl and Ba using 2 M HNO_3. Subsequently, REEs were collected in 6 M HCl and dried out. Then Ce was separated from the REE fraction after its transformation into Ce^{4+} using a solution of 10 M HNO_3 + $NaBrO_3$. The other REEs under the 3+ form are not retained into the LNspec resin using this solution. Finally, the Ce fraction is collected later in a 7 ml wash using 6 M HCl mixed with H_2O_2. The obtained Ce fractions were separated again from potential residues of Ba using AG50W-X8 columns, where 2 M HNO_3 allowed eluting the residual Ba before Ce collection in 6 M HCl. ICP-MS analyses of a small aliquot (1 %) of the Ce fractions confirmed the success of the separation step before analysis of isotopic ratios. The separation of Sm and Nd aliquots started also with isolation of the REE in the AG50W-X8 column. Then, separation of Nd and Sm was realised using diluted HCl (0.2 M and 0.5 M, respectively) in a LN-Spec column.

Cerium isotopes were measured using a Thermo Scientific Triton plus TIMS at University Clermont Auvergne using the technique described in Bonnand et al. (2020) and Israel et al. (2020). Ce isotopes are routinely measured in oxide forms using double Re filaments. An analytical run comprises 27 blocks of 20 cycles with 8.462 second integration time, and 60 seconds of baseline measurement before every cycle, such that each sample analysis lasted approximately two hours once the filament is hot enough to provide the desired signal. Corrections for (1) mass bias using $^{136}Ce/^{142}Ce = 0.01688$ (Makishima et al., 1986); (2) oxide and (3) the effect of the ^{140}Ce tailing on the ^{138}Ce signals were done offline following Israel et al. (2020). Repeated analyses of Ce AMES (Ce_{LMV} of Bonnand et al., 2020) reference material provided $^{138}Ce/^{142}Ce$ ratios of 0.2256992 ± 0.00000077 (34 ppm, n = 8; Table S4). We also obtained a $^{138}Ce/^{142}Ce$ of 0.02256408 ± 0.00000023 (n = 1) for BHVO-2. All these values are consistent with previously published values (Bonnand et al., 2020; Israel et al., 2020).

Isotopic measurements for Nd and Sm were carried out using a Thermo Scientific Neptune Multicollector ICP-MS in University Clermont Auvergne. For Nd isotopic measurement, the JNdi-1 reference material (Table S5) has been analysed after every 3 samples and values have been normalised to the published value of 0.512099 for $^{143}Nd/^{144}Nd$ (Garçon et al., 2018). We applied corrections for instrumental fractionation ($^{146}Nd/^{144}Nd = 0.7219$) and spike composition offline. After corrections, the BHVO-2 standard provided $^{143}Nd/^{144}Nd$ and $^{147}Sm/^{144}Nd$ ratios of 0.513019 ± 0.000018 and 0.1500 respectively, that are consistent with published values (Garçon et al., 2018; Li et al., 2012). External precisions (2 SD) are estimated at 0.5 epsilon unit for $^{143}Nd/^{144}Nd$ and 0.2 % for $^{147}Sm/^{144}Nd$ ratios.

For high-precision La/Ce ratio measurement, we gravimetrically prepared 11 synthetic solutions with fixed La/Ce ratios ranging between 0.3 and 1.3. Solutions were prepared from La and Ce standards solution (ASTASOL) with concentration known with a precision of 0.2 %. Three to five repetitive analyses of ^{139}La and ^{140}Ce counts in synthetic and natural solution using the Agilent Technologies 8900 QQQ-ICP-MS allowed precise determination of the La/Ce ratios of samples. The La/Ce ratios obtained by this technique are in good agreement with those calculated directly from trace element concentrations (Table S6), but this technique allows us to considerably improve the external precision (2 RSD) from > 2 % when the La/Ce ratio is calculated from trace element concentrations to 0.4 % (see Table S6). The La/Ce ratio obtained for the BHVO-2 standard is 0.4048 ± 0.0003, consistent within uncertainty with the value of 0.4053 ± 0.0004 determined by isotopic dilution (Schnabel et al., 2017). Measurements of La/Ce ratios using the two different methods (bulk trace element measurement and repeated analyses of La and Ce from the samples bracketed by synthetic solutions for which La/Ce ratios are known) are compared in Table S6.

4 Results

4.1 Petrography

4.1.1 Silicified volcanic rocks

Silicified volcanic rocks are greenish to dark-greyish in colour and are recognisable in the field by preserved magmatic features such as the pillows observed in the Theespruit, Komati and Hooggenoeg 3 sections (Figure 3a). They can also feature an ocelli texture as observed in Hooggenoeg 3 section, e.g. sample SK-HO13 (Figure 3b). In the Middle Marker and Mendon 1 sections, silicified volcanic rocks locally display a hydrothermally-induced "zebra" texture (Duchac and Hanor, 1987; Paris et al., 1985) composed of centimetre-scale bands of silicified volcanic rock that are interspaced with parallel quartz- and carbonate-bearing veins (Figure 3c).

The volcanic rocks are increasingly silicified from the base of sections (Figure 2) to the contact with the overlying sedimentary layers. Under the microscope, textures of least-silicified volcanic rocks reflect their volcanic origin while partially to completely silicified volcanic rocks do not show typical magmatic textures anymore (e.g. Figure 4b-d). In the least silicified volcanic rocks, olivine and pyroxene relicts, now replaced by epidote-dominated assemblages, are present in a matrix containing different oxides (chromite and Fe-Ti oxides), feldspars, carbonates and quartz (Figure 4b). Partially silicified volcanic rocks show a heterogeneous texture depicting millimetre-scale quartz-rich and quartz-poor zones reflecting different intensities of fluid circulation at this scale. The quartz-poor zones are rather dominated by phyllosilicates (muscovite and chlorite), oxides and epidote (Figure 4c). In most pervasively silicified volcanic rocks, magmatic minerals are almost completely replaced by a fine-grained (< 30 µm) quartz-dominated cement (Figure 4d). Variable amounts of carbonates, phyllosilicates, Fe-Ti oxides and sulfides (pyrite, arsenopyrite, chalcopyrite and pentlandite) are also disseminated in this quartz-rich cement. Automorphic chromite occurring in many silicified volcanic samples is considered as the only magmatic mineral that survived the silicification process, although chromite is also partially replaced by Fe-Ti-oxide in the pervasively silicified volcanic rocks.

The mineralogical assemblage of volcanic rocks from the Theespruit section reflects the amphibolite facies metamorphism constrained by previous studies (Cutts et al., 2014; Diener et al., 2005). At the base of the Theespruit section, volcanic rocks occur as amphibolites and are mostly composed of amphibole, carbonate, oxides and quartz. The upper part of the Theespruit volcanic unit appears as a chlorite-bearing schist (Figure 2a) made of alternating, sub-millimetre-scale quartz-rich and chlorite-rich layers that contain also garnet and Fe oxides.

4.1.2 Silicified clastic sedimentary rocks

Grey and black-and-white cherts commonly exhibit a clastic texture, with some pseudomorphs of detritic grains set in a microquartz matrix (containing also minor muscovite, chlorite, apatite, oxide and sulfide). These cherts may display a characterising normal grading pattern towards the upper levels of the sedimentary strata, where the amount of detrital pseudomorphs decreases (Figures 3d, 5). Detrital grain pseudomorphs show various morphologies ranging from slightly angular to rounded grains. They are mostly replaced by a quartz-dominated assemblage comprising also phyllosilicate (i.e. muscovite and chlorite), carbonates and oxide (Figure 4a-d). Quartz grains are often coarser in the clast relicts than the microquartz constituting the matrix. Within black-and-white cherts, white layers are generally coarser-grained and contain more phyllosilicates than black chert layers which are finer-grained and commonly contain blackish carbonaceous materials and oxides. Overall, the grey and black-and-white samples represent clastic sediments silicified after their deposition on the seafloor. These cherts still preserve some textural vestiges of their clastic origin such as the detrital pseudomorphs and grading patterns (Figure 5).

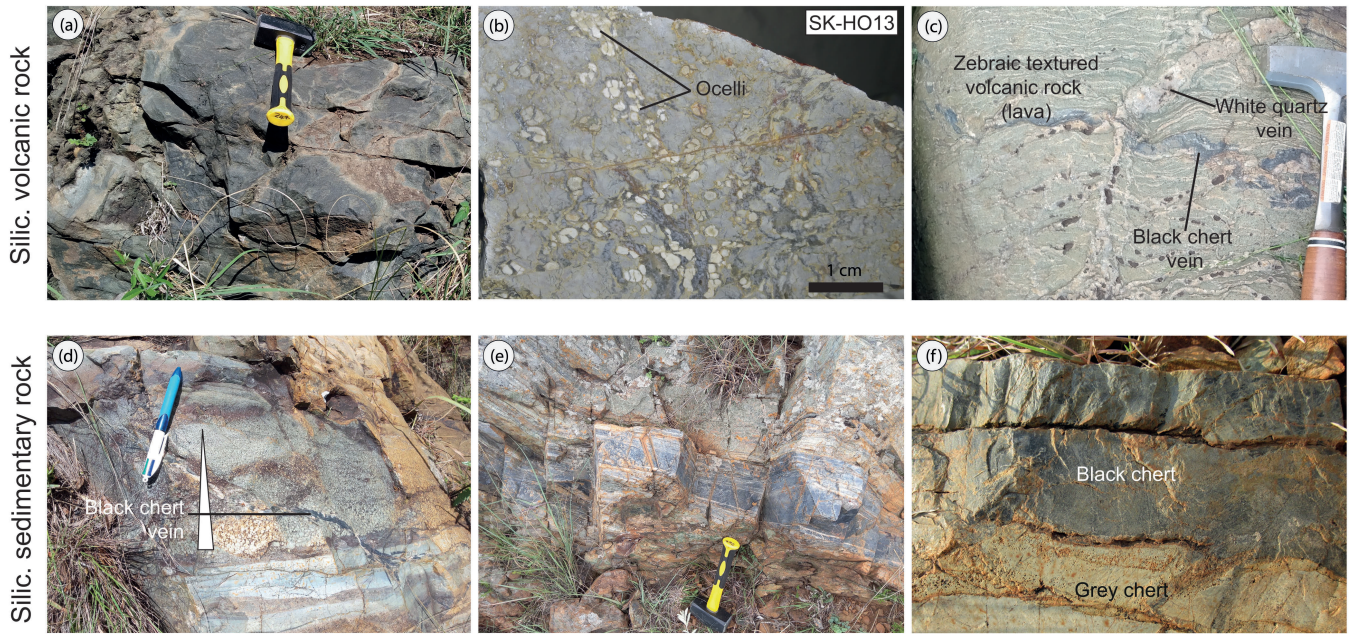

Figure 3. Representative outcrop aspects of silicified volcanic rocks and sedimentary lithofacies. (a) Pillows from the Theespruit Formation. (b) Ocelli-bearing silicified volcanic rock from the Hooggenoeg 3 Formation. (c) Zebra textured silicified volcanic rock from the Mendon 1 section showing sequences of silicified volcanic rocks and generally parallel white (quartz-rich) veins, although some veins cross-cut the zebra texture. (d) Bands of grey cherts with different clast grain sizes and possible grading (see white triangle pointing to the top of a graded layer) crosscut by a black chert vein in the Mendon 1 section. (e) Black-and-white chert showing decimetric to centimetric alternation of black and grey chert bands in the Middle Marker Unit. (f) Black chert overlying a grey chert band at the top of the Middle Marker section.

Black cherts (Figure 3f) are generally dominated by microquartz (> 90 vol %) but contain also carbonates, sulfides, oxides, carbonaceous materials and minor apatite in all sections. Unlike grey or black-and-white cherts, they do not feature evident clastic features and are free of visible clast relicts.

Finally, metasedimentary schists (not illustrated) were only observed in the Theespruit section that underwent amphibolite-facies metamorphism (Figure 2a). These metasedimentary schists are made of quartz, sericite and oxide phases accompanied by accessory feldspar and garnet. A preferred orientation of sericite in the samples controls the schistosity. Besides the schistose aspect of these metasedimentary schists, another factor differentiating them from "cherts" is that the proportion of silica in the metasedimentary schists does not exceed ~ 70 vol %.

4.1.3 Veins

Two main types of veins are identified in the silicified rocks that we analysed. The first type consists of quartz veins that are decimetric to sub-millimetric wide (Figures 3c,d, 5). The quartz grains filling these veins are generally coarser than the microquartz constituting silicified volcanic and sedimentary rocks that they intrude. In addition to the dominant quartz, these veins sometimes contain carbonates, in variable proportions (calcite or ankerite visually estimated to reach 50 vol % locally), with common inclusions of quartz grains (see Figure 7e,f). This implies that quartz and carbonate grew coevally in the veins.

The second type of veins observed in the samples consists of clay-oxide veins crosscutting both the microquartz matrix and the quartz-veins, which suggests that these veins formed after hydrothermal silicification near the Paleoarchean seafloor. These clay-oxide veins do not exceed the millimetric scale in size (e.g. Figure 5).

4.2 Equilibrium temperatures

Here we present the results of three different thermometers that we analyzed to estimate the equilibrium temperatures recorded by the Onverwacht silicified volcanic and sedimentary rocks above the Komati Fault and their relationship with the silicification process. These thermometers are (1) the Raman spectrometry of carbonaceous material, (2) the chemistry of chlorite and (3) the equilibrium oxygen isotope fractionation between quartz and carbonate phases. The peak temperature of the amphibolite-facies metamorphism that affected the Theespruit Formation below the Komati Fault was previously estimated to exceed 550 °C based on associated mineral assemblages (i.e. staurolite-garnet-kyanite in metasedimentary rocks, and hornblende-epidote-garnet in metamafic rocks; Cutts et al., 2014; Diener et al., 2005), and is not re-assessed here. While Raman spectra of carbonaceous materials were acquired for silicified sedimentary rock samples from four different sections above the Komati Fault (i.e. Middle Marker, Hooggenoeg 3, Hooggenoeg 4 and Mendon 1 sections), chlorite thermometry and oxygen isotope thermometry were only performed for samples from the lower Middle Marker and the uppermost Mendon sections.

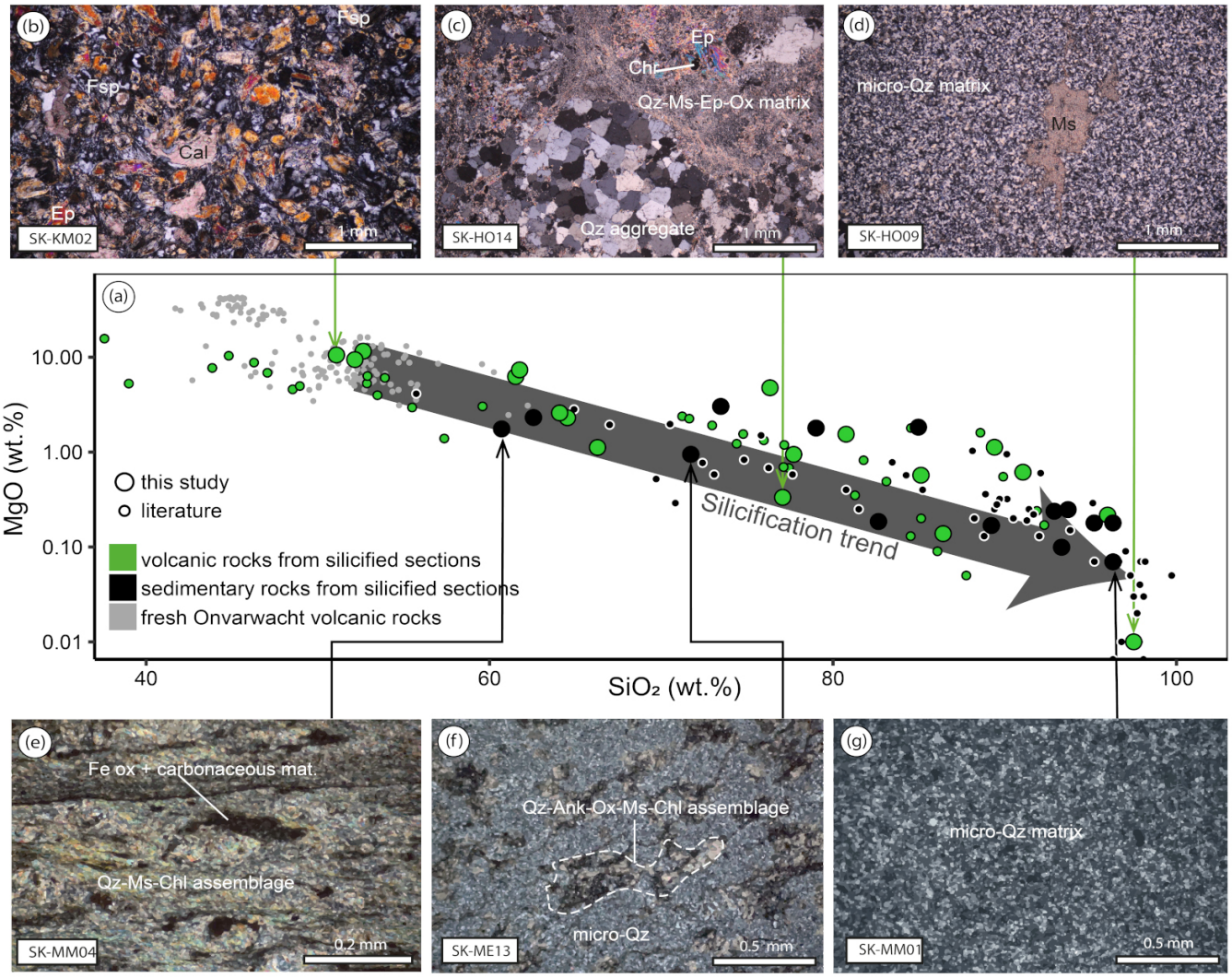

Figure 4. (a) SiO_2 versus MgO diagram showing the trend followed by volcanic and sedimentary rocks during their silicification near the Paleoarchean seafloor. (b) to (d): petrographic microphotographs depicting the textural evolution of volcanic rocks observed from least silicified to highly silicified specimens. (e) to (g): petrographic microphotographs showing the textural evolution of sedimentary rocks from least silicified to the highly silicified specimen. Previously analysed silicified volcanic and sedimentary rocks from the Onverwacht Group that are shown in panel (a) for comparison were compiled from Abraham et al. (2011), Geilert et al. (2014), Hofmann et al. (2013), Hofmann and Harris (2008), Ledevin et al. (2014, 2019), Rouchon et al. (2009), Rouchon and Orberger (2008). The compositions of fresh volcanic rocks from the Onverwacht Group were taken from Chavagnac (2004), Furnes et al. (2012), Lahaye et al. (1995), Parman et al. (2001), Puchtel et al. (2013), Schneider et al. (2019).

4.2.1 Raman spectrometry of carbonaceous material

Details about Raman spectra of measured carbonaceous materials are provided in Table S7 and representative spectra are illustrated in Figure 6a (with all acquired spectra illustrated in Figure S5). These data allow us to calculate peak temperatures of 361 ± 13 °C in the Middle Marker cherts (SK-MM06, 2 SD, n = 11), 333 ± 18 °C in the Hooggenoeg 3 chert (SK-HO03, n = 9), 343 ± 15 °C in the Hooggenoeg 4 chert (SK-HO25, n = 10) and 352 ± 13 °C in the Mendon 1 chert (SK-M113, n = 15). Average temperatures per individual sample cover a narrow range of 333 to 366 °C and internal standard deviations are lower than 30 °C. Thus carbonaceous materials from the Onverwacht cherts equilibrated at similar temperatures of ~350 °C (average = 347 ± 40 °C). An uncertainty of 50 °C is generally considered for this technique. Thus, the temperature obtained here is consistent with low-grade metamorphic conditions (300–400 °C) constrained by previous analyses of the Raman spectra of carbonaceous material in Onverwacht cherts (Alleon et al., 2021; Hofmann et al., 2013; Tice et al., 2004; van Zuilen et al., 2007).

4.2.2 Chlorite thermometry

Equilibrium temperatures were determined based on compositional maps of chlorite using the dynamic method of Vidal et al. (2016) and the X-map Tools software (Lanari et al., 2014). An example of a temperature map and selected zones for the determination of equilibrium temperature are illustrated in Figure 6b while all other maps are provided in

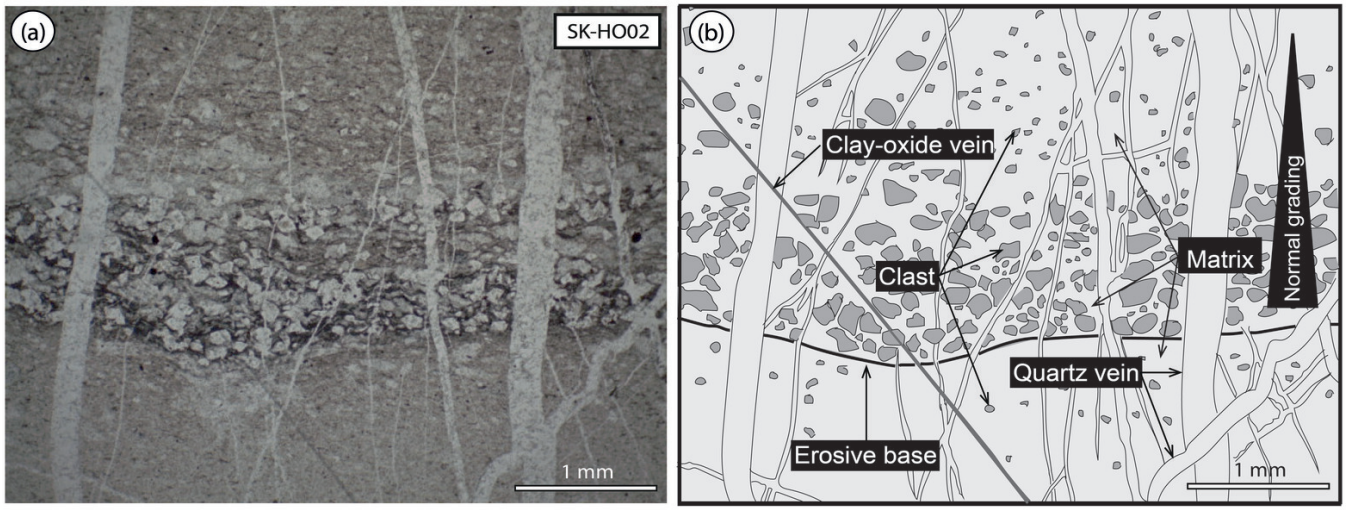

Figure 5. Illustration of clast relicts, matrix and cross-cutting veins in the black-and-white SK-HO02 chert sample from the Hooggenoeg 3 section. Note the presence of an erosive base and the normal grading of clasts upwards in the sedimentary layer. (a) represents a microphotograph and (b) is an interpretation sketch drawing interpreting this microphotograph and illustrating the different quartz types and veins that are present in the rock.

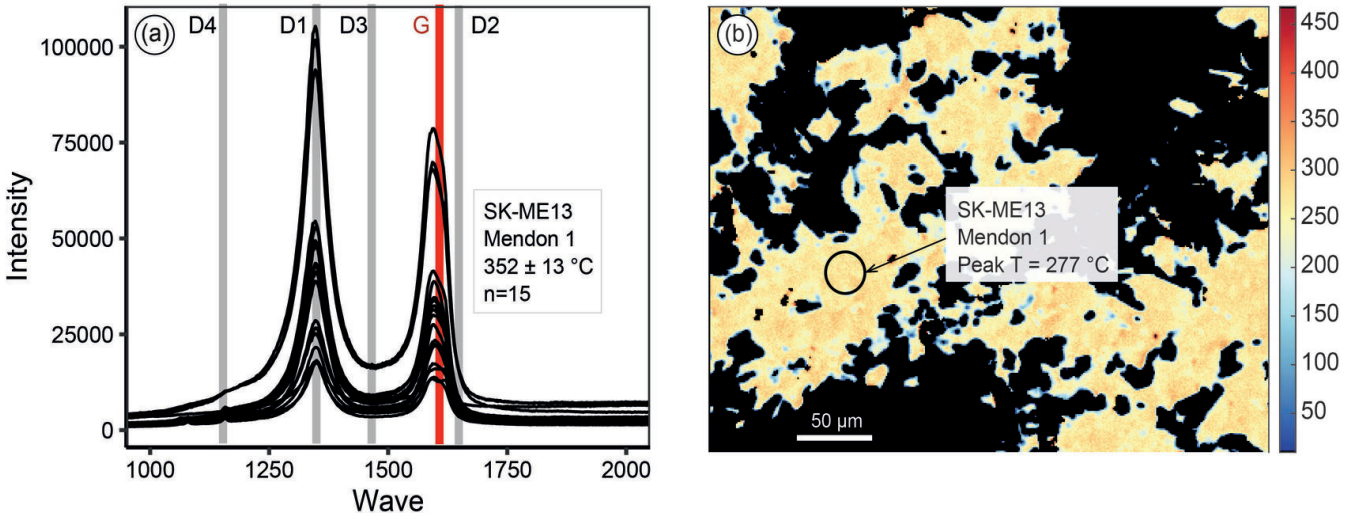

Figure 6. An example of (a) Raman spectra of carbonaceous materials with associated equilibrium temperatures and (b) thermal maps of chlorite obtained in this study. In panel (a), the location of the different peaks of carbonaceous materials are shown by grey and black lines and reported temperatures are average values and errors correspond to 2 SD from measurements of 9 to 15 carbonaceous materials in individual samples. The D1, D2, D3 and D4 peaks shown in panel (a) are positions of Raman shifts related to disorganised carbon that transforms into organised graphite (G peak) depending on the temperature of re-equilibration; the relative importance of these peaks in any carbonaceous material allows determining the equilibrium temperature retrospectively (see Section 3.1 for further detail). In panel (b), the map derived from treatment of compositional maps using XmapTools software and the black circle corresponds to the area that was selected to calculate equilibrium temperatures. Notably, chlorite thermometry cannot allow a better precision than a 2 SD of 50 °C in estimated equilibrium temperatures (Vidal et al., 2016). The scale in panel (b) corresponds to temperature in °C.

the Figure S6. The temperatures displayed by all chlorite rims are lower than those observed in cores due to higher SiO_2 and Al_2O_3 contents in the rims. Rim temperatures are considered as unrepresentative of chlorite equilibration because they were more prone to modification by late-stage processes such as weathering. Equilibrium temperatures calculated based on chlorite composition for Middle Marker and Mendon 1 samples are similar and cover a narrow range extending between 277 and 292 °C. Because analytical uncertainties of the chlorite thermometry generally exceed 50 °C of error (2 SD; Bourdelle, 2021), we consider that all the analysed chlorites equilibrated at an average temperature of 280 ± 50 °C.

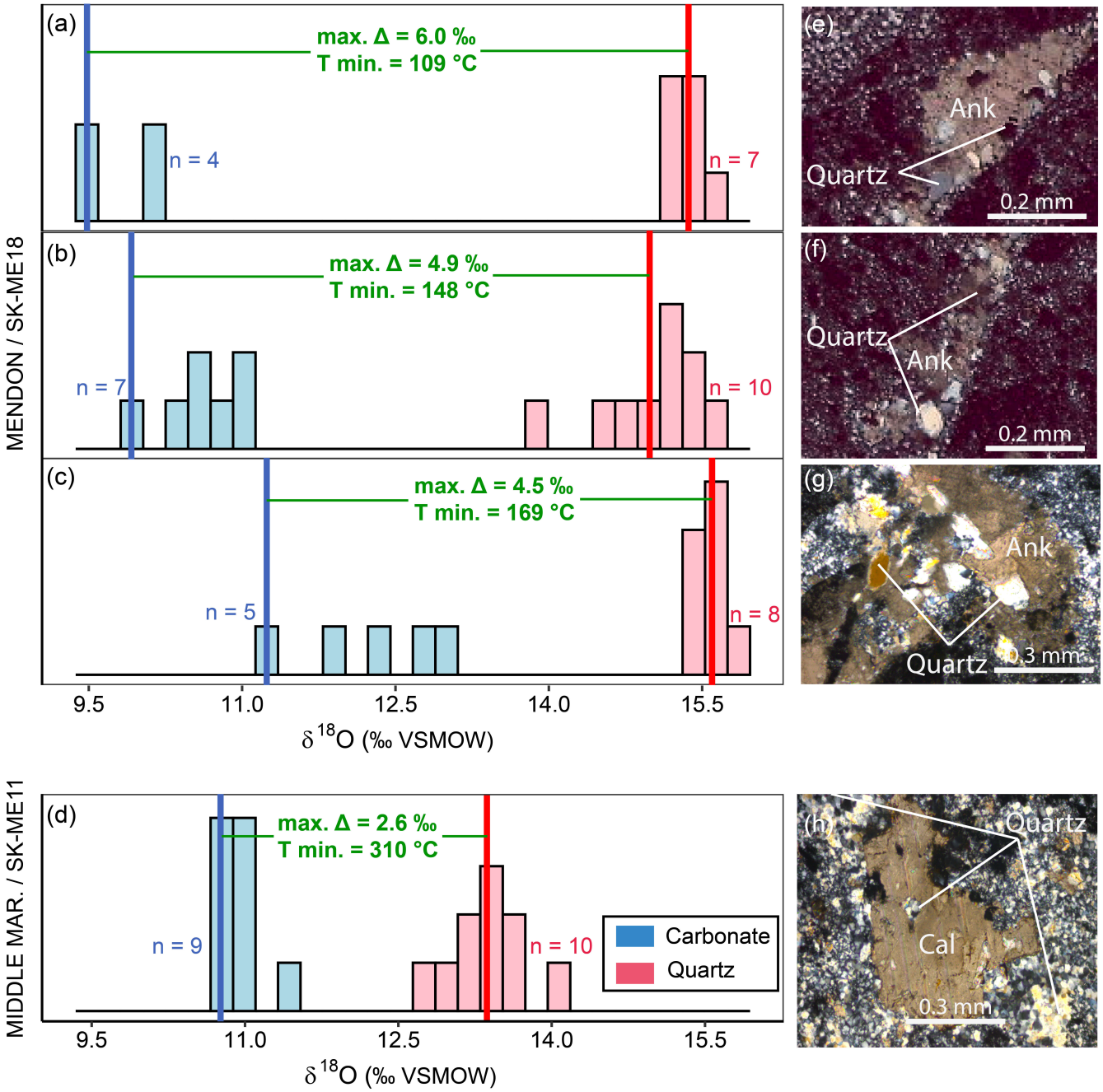

Figure 7. Histograms showing the distribution of $\delta^{18}O$ values and equilibrium temperatures obtained from analysed quartz (reddish) and carbonate (bluish) assemblages. (a), (b) and (c) present results of analyses in individual assemblages of the silicified volcanic rock sample SK-ME18 of the Mendon section. (d) presents results obtained from the single assemblage of the silicified volcanic rock sample SK-MM11 that we analysed. Vertical lines show mean quartz $\delta^{18}O$ values (red) and minimum carbonate $\delta^{18}O$ values (blue). The reported minimum temperatures were calculated using the following equation: maximum $\Delta = 0.87(\pm 0.06) \times 10^6/T^2$ (Clayton et al., 1972; Sharp and Kirschner, 1994), with maximum Δ = mean $\delta^{18}O_{quartz}$ - minimum $\delta^{18}O_{carbonate}$. (e), (f), (g) and (h) show the petrography of the quartz-carbonate assemblages whose O isotope compositions are respectively displayed in (a), (b), (c) and (d).

4.2.3 Quartz-carbonate oxygen isotope thermometry

At equilibrium, the fractionation of oxygen isotopes between quartz and carbonate phases precipitated from the same fluid ($\Delta^{18}O_{quartz\text{-}carbonate} = \delta^{18}O_{quartz} - \delta^{18}O_{carbonate}$) depends mainly on the temperature of the system (Clayton et al., 1972; Sharp and Kirschner, 1994). We use $\Delta^{18}O_{quartz\text{-}carbonate}$ for quartz and carbonates from two samples of silicified volcanic rocks (Middle Marker SK-MM11 and Mendon 1 SK-ME18) to determine their temperature of equilibration and constrain the temperature of silicifying hydrothermal fluids (Figure 7a-h). For the SK-ME18 sample, we analysed two quartz-ankerite assemblages occurring in a vein (Figure 7a,b,e,f) and one assemblage from the matrix (Figure 7c,g). For the SK-MM11 sample, we analysed one quartz-calcite assemblage from the matrix (Figure 7c,e). Texturally, quartz is inclusive into carbonate

Table 1. Summary of acquired thermometric and oxygen isotope data. Spectra of carbonaceous material analysed to calculate temperatures of equilibration were obtained by Raman spectroscopy. Major element compositions of chlorites used to calculate temperatures of equilibration were obtained by electron probe micro-analysis (EPMA). Oxygen isotope compositions of quartz and carbonate were obtained by secondary ion mass-spectrometry (SIMS) and are expressed in permil difference from VSMOW reference. Abbreviations: b=black, g=grey, bw=black-and-white.

Section	Proxy	Sample	Rock type	Zone / Assemblage	Mean $\delta^{18}O$ quartz ‰	Mean $\delta^{18}O$ carb. ‰	Min. $\delta^{18}O$ carb. ‰	Mean T ± 2 SD (°C)	Minimum T (°C)
Mendon 1	Carbonaceous mat.	SK-ME11	b chert					352 ± 25 (n=15)	
Mendon 1	Chlorite	SK-ME13	g chert					277 ± 50	
Mendon 1	Chlorite	SK-ME24	volcanic rock					292 ± 50	
Mendon 1	Quartz-ankerite	SK-ME18	volcanic rock	1	15.37 ± 0.28	9.79 ± 0.85	9.40		109
Mendon 1	Quartz-ankerite	SK-ME18	volcanic rock	2	14.75 ± 1.91	10.53 ± 0.74	9.85		148
Mendon 1	Quartz-ankerite	SK-ME18	volcanic rock	3	15.57 ± 0.31	12.21 ± 1.48	11.10		169
Hooggenoeg 4	Carbonaceous mat.	SK-HO25	g chert					343 ± 24 (n=9)	
Hooggenoeg 3	Carbonaceous mat.	SK-HO03	g chert					326 ± 28 (n=10)	
Middle Marker	Carbonaceous mat.	SK-MM06	bw chert					361 ± 44 (n=11)	
Middle Marker	Chlorite	SK-MM05		1				292 ± 50	
Middle Marker	Chlorite	SK-MM05	bw chert	2				285 ± 50	
Middle Marker	Quartz-calcite	SK-MM11	volcanic rock	4	13.37 ± 0.68	10.94 ± 0.46	10.69		310

in all analysed assemblages (Figure 7e-h), suggesting either co-precipitation of the two minerals from the same fluid or precipitation of carbonate after quartz. Analysed quartz is generally coarser than matrix microquartz and, accordingly, does not represent a portion of the matrix detached by carbonate-saturated fluids after silicification (Figure 7a-h). No remnant or inclusion of another mineral apart from quartz is observed in analysed carbonates, supporting direct precipitation of carbonate from the fluid rather than its formation through replacement of another pre-existing mineral. We interpret these petrographic observations as inferring co-precipitation of analysed quartz and carbonates from the same fluid, which justifies estimating equilibrium fluid temperature from their isotopic composition.

Oxygen isotope compositions of analysed quartz and carbonate spots are provided in Table S8 and summarised in Table 1 together with calculated temperatures. In the three quartz-ankerite assemblages of SK-ME18 sample, quartz $\delta^{18}O$ values range respectively from 15.1 to 15.6 ‰, 13.9 to 15.5 ‰ and 15.4 to 15.7 ‰ (Figure 7a-c). The $\delta^{18}O$ values of ankerites associated with these quartz range from 9.4 to 10.2 ‰, 9.9 to 10.9 ‰ and 11.1 to 12.9 ‰, respectively. In the Middle Marker sample SK-MM11, quartz $\delta^{18}O$ values range from 12.8 to 14.0 ‰ and calcite $\delta^{18}O$ values range from 10.7 and 11.5 ‰ and (Figure 7d). Notably, ankerite $\delta^{18}O$ values in SK-ME18 sample show an important variation spanning ∼3.5 ‰, with average ankerite $\delta^{18}O$ per assemblage ranging from 9.8 to 12.2 ‰. In contrast, average quartz $\delta^{18}O$ per assemblage is less variable and only ranges between 14.8 and 15.6 ‰ in sample SK-ME18 (Table 1, Figure 7a-c). We ascribe the important variation of ankerite $\delta^{18}O$ towards higher values in this sample to partial resetting during a later thermal event (metamorphism), and we accordingly consider for each analysed assemblage a least-reset maximum $\Delta^{18}O_{quartz\text{-}carbonate}$ (difference between average quartz $\delta^{18}O$ and minimal carbonate $\delta^{18}O$) to calculate the minimal temperature of equilibrium before metamorphism (Table 1, Figure 7a-d). For the SK-ME18 sample, the least-reset maximum $\Delta^{18}O_{quartz\text{-}carbonate}$ values for the three different assemblages are 6.0, 4.9, 4.5 ‰, which correspond to temperatures of 109, 148 and 169 °C. For the SK-MM11 quartz-calcite assemblage, we obtain a maximum $\Delta^{18}O_{quartz\text{-}carbonate}$ of 2.6 ‰ corresponding to a temperature of 242 °C. Considering the external analytical uncertainty (2 SD) of ∼0.5 ‰ obtained in this study for $\delta^{18}O$ values, an error of ∼50 °C is estimated for the lowest temperature.

We interpret the range of equilibrium temperatures (∼110 to ∼350 °C) obtained from the three different thermometers analysed in this study (Table 1) as recording two different episodes of thermal equilibration in analysed rocks. The first episode corresponds to co-precipitation of quartz and carbonate from the same fluid at a relatively low temperature which we quantify to ∼110 ± 50 °C using the maximum $\Delta^{18}O_{quartz\text{-}carbonate}$ in one quartz-ankerite assemblage of sample SK-ME18 (Figure 7a). We associate this relatively low temperature with hydrothermal silicification near the Paleoarchean

seafloor. The second episode of thermal equilibration corresponds to re-equilibration during a subsequent thermal event at ~350 ± 50 °C, as recorded by the Raman spectra of carbonaceous material (Figures 6a and Figure S5). Within error consistent with this temperature is the chlorite equilibrium temperature of ~280 ± 50 °C (Figure 6b). All intermediate temperatures obtained from quartz-carbonate assemblages (Figures 7a-d) are ascribed to incomplete re-equilibration during the higher temperature episode.

4.3 Bulk-rock geochemistry

4.3.1 Major and trace element compositions

The major and trace element compositions of silicified rocks that we analysed are provided in Table S9 and Table S10, and element concentrations and ratios discussed in this manuscript are presented in Table 2. With the increase of microquartz volume due to silicification, SiO_2 concentration increases from the typical composition of fresh volcanic rocks from the Onverwacht Group to more than 96 wt %. The concentration of other major elements such as MgO, Fe_2O_3, CaO and MnO decreases beyond the field of fresh Onverwacht volcanic rocks (e.g. Figure 4a), as also previously observed by Hofmann and Harris (2008). Additionally, in the silicified volcanic and sedimentary rocks, Zr/Hf (27.1–47.9) and Y/Ho (20.8–35.9) ratios, which are generally used to distinguish seawater-precipitated cherts from silicified clastic sedimentary rocks (Bau, 1996), remain within the range of fresh Onverwacht volcanic rocks at any SiO_2 concentration (Figures 8a,b). Contrastingly, the Sm/Nd ratio, that controls the evolution of radiogenic ^{143}Nd isotope abundance, shows a slight decrease with increasing SiO_2 concentration both in the silicified volcanic rocks and in the silicified sedimentary rocks, with values ranging between 0.16 and 0.39 (Figure 8c). The Lu/Hf ratio, that controls the evolution of radiogenic ^{177}Hf abundance, ranges between 0.02 and 0.10 in silicified volcanic and sedimentary rock samples, extending to both lower and higher values than fresh Onverwacht volcanic rocks (Figure 8d). Additionally, compared to the composition of fresh volcanic rocks from the Onverwacht Group, higher values of K_2O, Rb, Ba, Sr versus Zr ratios occur in silicified volcanic and sedimentary rocks (e.g. higher K_2O/Zr and Rb/Zr shown in Figure 8e,f). This corroborates the previously proposed sequestration of alkalis during hydrothermal silicification of Paleoarchean volcanic and sedimentary rocks.

The chondrite-normalised (CN) and post-Archean Australian Shale-normalised (PAAS) patterns of rare elements (REE) in the analysed samples are shown in Figure 9. Chondrite-normalised REE patterns of the analysed samples (Figure 9a,b) are flat to positively sloped (Pr/Yb_{CN} = 0.4–29.6), which corresponds to negatively sloped PAAS-normalised patterns (Figure 9c,d). The REE content of all analysed samples remain within the field of fresh volcanic rocks and granitoids from the Barberton. Yet, the samples depict a rough decrease of REE content with increasing SiO_2 concentration. While all samples but one display a positive Eu anomaly on chondrite-normalised REE patterns (Eu/Eu^*_{CN} = 0.5–2.4, where $Eu/Eu^*_{CN} = Eu_{CN} / (Sm_{CN}^2 \times Tb_{CN})^{1/3}$), chondrite-normalised patterns of the silicified volcanic and sedimentary rock samples display both positive and negative Eu anomalies (Eu/Eu^*_{CN} = 0.3–1.5). Two out of the three metasedimentary schist samples from the Theespruit section display negative Eu anomalies down to 0.44. Negative Ce anomalies ($Ce/Ce^*_{PAAS} = Ce_{PAAS} / (Pr_{PAAS}^2 / Nd_{PAAS})$) are common in our sample set (for example, Ce/Ce^*_{PAAS} = 0.39 and 0.51 in samples SK-HO01 and SK-HO05 respectively). Positive PAAS-normalised Ce anomalies were also measured in the Middle Marker volcanic rock sample SK-MM10 (Ce/Ce^*_{PAAS} = 1.34), Middle Marker chert sample SK-MM04 (Ce/Ce^*_{PAAS} = 1.30) and in the Theespruit metasedimentary schist sample SK-TH11 (Ce/Ce^*_{PAAS} = 1.44). Finally, Y/Ho ratios of analysed silicified rock samples range between 21.3 and 36.0 and reflect minor Y anomalies on REE patterns.

4.3.2 Sm-Nd and La-Ce isotopic compositions

Results obtained for the two long-lived ^{138}La-^{138}Ce and ^{147}Sm-^{143}Nd systematics in eleven representative samples (3 silicified volcanic rocks and 8 silicified sedimentary rocks) and the BHVO-2 reference basalt are presented in Table 3 and Figure 10. Values for $^{138}La/^{142}Ce$ ratios are calculated considering the equation $^{138}La/^{142}Ce = La/Ce \times 0.0082236$ (calculated considering masses and isotopic abundances reported in Schnabel et al., 2017). The silicified volcanic rocks show a narrow range of $^{143}Nd/^{144}Nd$ and $^{138}Ce/^{142}Ce$ ratios. Silicified sedimentary rocks evolve from the composition of silicified volcanic rocks to higher $^{138}Ce/^{142}Ce$ and lower $^{143}Nd/^{144}Nd$ ratios. The $^{138}La/^{142}Ce$ generally cover a narrow range in samples that are free of significant Ce anomalies. Samples that display a significantly negative Ce anomaly are characterised by considerably higher $^{138}La/^{142}Ce$ ratios, whereas the opposite is observed for samples that display positive Ce anomalies.

In a $^{147}Sm/^{144}Nd$ vs $^{143}Nd/^{144}Nd$ isochron diagram, samples are aligned along a theoretical 3.4 Ga Sm-Nd isochron, except two samples that are shifted on the left side (Figure 10a). These samples are SK-HO01 (volcanic rock sample) and SK-HO05 (chert), that display negative Ce anomalies (Figure 10c). For the La-Ce systematics, all samples except four plot close to the theoretical 3.4 Ga isochron (Figure 10b). The four samples falling off the regression line are those characterised by negative (SK-HO01, SK-HO05) or positive Ce anomalies (SK-TH11 and SK-MM04; Figure 10c). These samples also have extreme initial ε_{Nd} and ε_{Ce} values when back-calculated to 3.4 Ga with values up to +27 and down to -27, respectively. Such values confirm that measured parent/daughter ratios cannot be used to correct from radiogenic ingrowth because they have been modified since the rock emplacement. More importantly, we note that rocks from the same group have relatively close Ce and Nd isotopic composition whether they display Ce anomalies or not. This suggests that the Ce anomalies were generated relatively recently.

Of the eleven samples for which we measured ^{138}La-^{138}Ce and ^{147}Sm-^{143}Nd isotopic composition, five samples

Table 2. Selected major and trace element concentration ratios in analysed silicified lavas and sediment samples. Major element concentrations were determined by X-ray Fluorescence (XRF). Trace element concentrations were obtained by QQQ-ICPMS. Abbreviations: b=black, g=grey, bw=black-and-white, bdl=below detection limit, metased.=metasedimentary. SiO_2, Mg and K_2O are expressed in wt.% whereas the trace elements Zr, Rb, Y, Ho, Sm, Nd, Lu and Hf are in ppm. $Ce/Ce^*_{PAAS} = Ce_{PAAS} / (Pr_{PAAS}{}^2 / Nd_{PAAS})$. $Eu/Eu^*_{CN} = Eu_{CN} / (Sm_{CN}{}^2 \times Tb_{CN})^{1/3}$.

Sample	Latitude	Longitude	Section	Lithology	SiO_2	MgO	K_2O/Zr	Rb/Zr	Y/Ho	Zr/Hf	Sm/Nd	Lu/Hf	Eu/Eu^*_{CN}	Ce/Ce^*_{PAAS}
SK-TH05	-25.9984604	30.8349333	Tjakastad	volcanic rock	61.5	6.25	0.0025	0.04	24.3	38.2	0.224	0.123	1.90	0.83
SK-TH07	-25.9984604	30.8349333	Tjakastad	volcanic rock	77.7	0.95	0.0193	0.02	26.3	47.9	0.263	0.103	0.55	0.95
SK-TH11	-25.9984604	30.8349333	Tjakastad	metased. schist	60.7	1.75	0.0069	0.17	24.2	33.4	0.159	0.047	0.84	1.39
SK-TH12	-25.9984604	30.8349333	Tjakastad	metased. schist	79.0	1.79	0.0039	0.14	30.4	33.5	0.159	0.077	0.70	0.92
SK-TH14	-25.9984604	30.8349333	Tjakastad	metased. schist	71.7	0.95	0.0111	0.26	28.5	36.4	0.185	0.016	1.79	0.95
SK-TH10	-25.9984604	30.8349333	Tjakastad	b chert	85.0	1.83	0.0009	0.67	27.0	37.8	0.230	0.100	1.69	0.92
SK-MM01	-25.9615500	30.8104833	Middle M.	bw chert	95.2	0.18	0.0094	0.30	20.8	42.3	0.212	0.027	1.40	0.84
SK-MM06	-25.9615500	30.8104833	Middle M.	bw chert	93.7	0.25	0.0664	1.95	27.9	41.8	0.256	0.085	1.72	1.03
SK-MM08	-25.9615500	30.8104833	Middle M.	bw chert	96.3	0.07	0.0110	0.34	21.3	42.2	0.183	0.016	1.44	0.80
SK-MM04	-25.9615500	30.8104833	Middle M.	bw chert	62.6	2.31	0.1126	3.49	26.3	33.5	0.319	0.160	1.39	1.24
SK-MM10	-25.9615500	30.8104833	Middle M.	volcanic rock	61.7	7.35	0.1012	2.84	27.5	32.8	0.306	0.143	1.39	1.34
SK-MM11	-25.9615500	30.8104833	Middle M.	volcanic rock	96.0	0.22	0.0407	1.15	28.1	47.0	0.295	0.706	0.95	1.23
SK-KM02	-25.9615500	30.8104833	Middle M.	volcanic rock	51.1	10.55	0.0210	0.18	26.1	36.8	0.314	0.192	2.14	0.94
SK-HO01	-25.9430878	30.8796744	Hoogg. 3	volcanic rock	76.3	4.76	0.0038	0.24	22.5	32.5	0.250	0.170	1.47	0.39
SK-HO05	-25.9430878	30.8796744	Hoogg. 3	bw chert	93.3	0.10	0.2172	6.83	30.2	27.1	0.171	0.051	1.89	0.51
SK-HO09	-25.9430878	30.8796744	Hoogg. 3	volcanic rock	97.5	bdl	0.1698	5.71	30.8	35.5	0.214	0.045	2.40	0.43
SK-HO12	-25.9430878	30.8796744	Hoogg. 3	volcanic rock	86.4	0.14	0.0920	4.23	28.6	33.5	0.261	0.195	1.76	0.99
SK-HO13	-25.9430878	30.8796744	Hoogg. 3	volcanic rock	85.1	0.57	0.0126	0.41	24.2	36.3	0.276	0.029	1.74	0.94
SK-HO14	-25.9430878	30.8796744	Hoogg. 3	volcanic rock	77.1	0.33	0.0263	0.60	26.8	36.9	0.247	0.084	1.43	0.92
SK-HO20	-25.9430878	30.8796744	Hoogg. 4	volcanic rock	52.6	11.56	0.0242	0.86	26.9	35.2	0.342	0.273	1.26	0.87
SK-HO21	-25.9430878	30.8796744	Hoogg. 4	volcanic rock	52.2	9.43	0.0052	0.12	25.8	34.0	0.319	0.396	1.62	0.62
SK-HO25	-25.9430878	30.8796744	Hoogg. 4	g chert	96.3	0.18	0.0093	0.31	25.5	40.1	0.218	0.016	1.33	0.86
SK-HO26	-25.9430878	30.8796744	Hoogg. 4	bw chert	89.2	0.17	0.0577	1.86	29.0	28.7	0.240	0.016	2.15	0.92
SK-ME10	-25.9144470	30.9307870	Mendon	bw chert	82.6	0.19	0.0103	0.36	29.7	42.6	0.268	0.894	2.30	1.01
SK-ME11	-25.9144470	30.9307870	Mendon	b chert	92.9	0.24	0.0955	2.95	27.3	36.7	0.225	0.164	1.84	0.91
SK-ME13	-25.9144470	30.9307870	Mendon	g chert	73.5	3.03	0.0730	2.95	27.3	34.5	0.271	0.264	1.68	0.97
SK-ME17	-25.9144470	30.9307870	Mendon	volcanic rock	89.4	1.12	0.2183	6.87	31.1	30.2	0.209	0.716	1.98	1.03
SK-ME20	-25.9144470	30.9307870	Mendon	volcanic rock	80.8	1.54	0.3207	10.43	36.0	28.4	0.389	1.098	2.23	1.12
SK-ME24	-25.9144470	30.9307870	Mendon	volcanic rock	91.1	0.61	0.1703	5.55	29.1	35.4	0.211	0.358	1.74	0.47
SK-ME26	-25.9144470	30.9307870	Mendon	volcanic rock	66.3	1.12	0.0280	0.73	24.4	34.8	0.178	0.044	1.58	0.95
SK-ME27	-25.9144470	30.9307870	Mendon	volcanic rock	64.5	2.30	0.0211	0.55	25.1	34.9	0.207	0.047	1.28	0.77

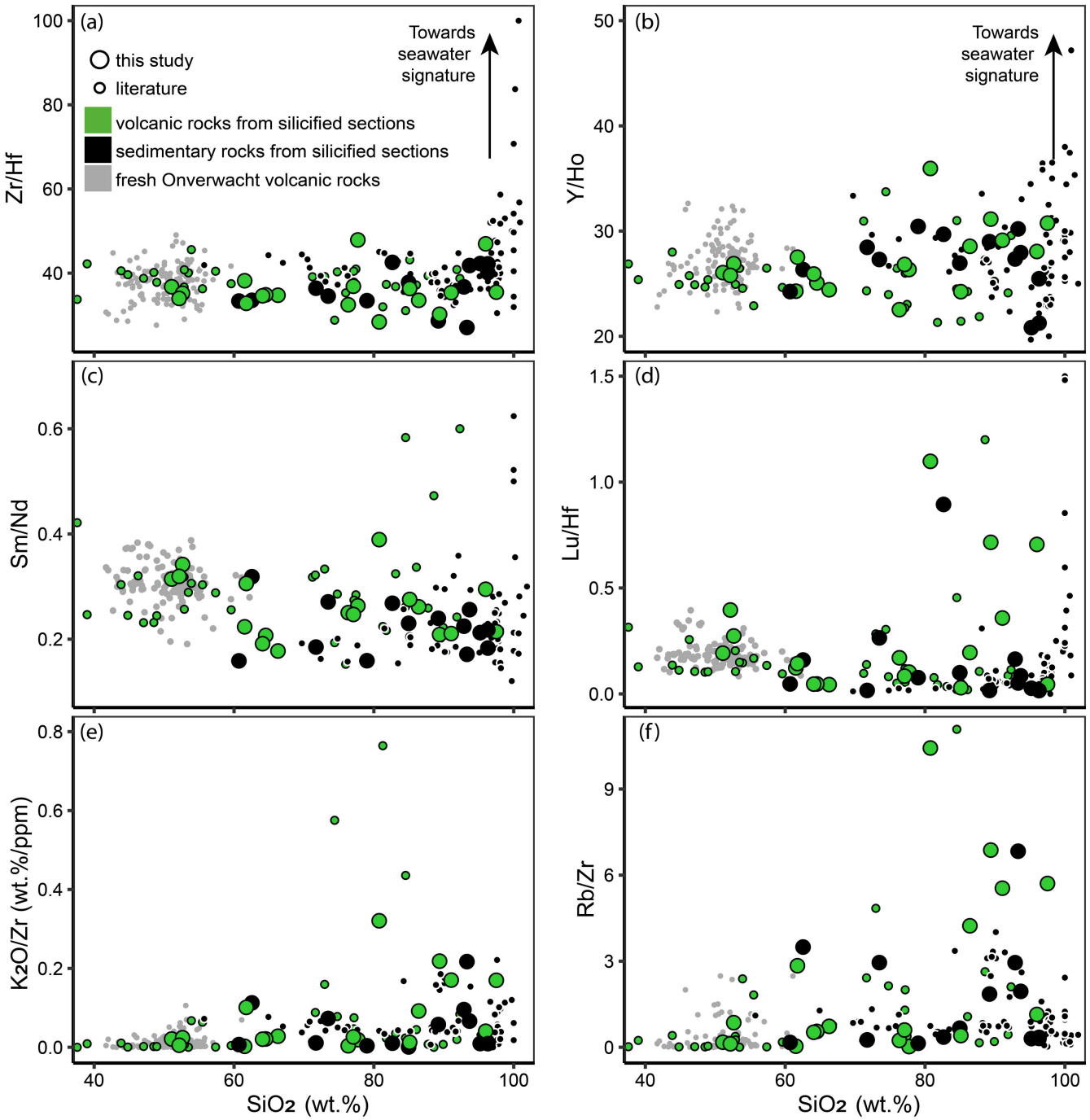

Figure 8. Evolution of selected elemental ratios with increasing SiO_2 concentration. (a) and (b): SiO_2 versus Zr/Hf and Y/Ho ratios for which silicified volcanic rocks generally remain within the range of fresh volcanic rocks for these ratios. (c): SiO_2 versus Sm/Nd showing that this ratio decreased slightly during silicification. (d): SiO_2 versus Lu/Hf ratio showing significantly variable Lu/Hf ratios in silicified volcanic (and sedimentary) rocks compared to fresh volcanic rocks. (e) and (f): SiO_2 versus K_2O/Zr and Rb/Zr ratio. We note higher K_2O/Zr and Rb/Zr ratios in silicified rocks compared to fresh volcanic rocks. References for the comparison data compiled from previous studies are given in Figure 4 caption.

have a negligible Ce anomaly with Ce/Ce^*_{PAAS} ranging between 0.92 and 0.95. The ^{138}La-^{138}Ce and ^{147}Sm-^{143}Nd isotope systematics of these five samples define respective errorchrons of 3.9 ± 0.6 Ga and 3.7 ± 1.1 Ga (see Figure S7). The large age errors calculated from the regressions in isochron plots are likely due to a combined influence of the limited number of fresh samples (only five), their slightly different ages (Table 3) and potential initial isotopic heterogeneities. These ages remain within error (although large ones) consistent with the formation of the Onverwacht Group between 3.5 and 3.3 Ga ago, despite being slightly older.

5 Discussion

The petrographic, thermometric and geochemical data reported in this study offer a unique opportunity to unravel the

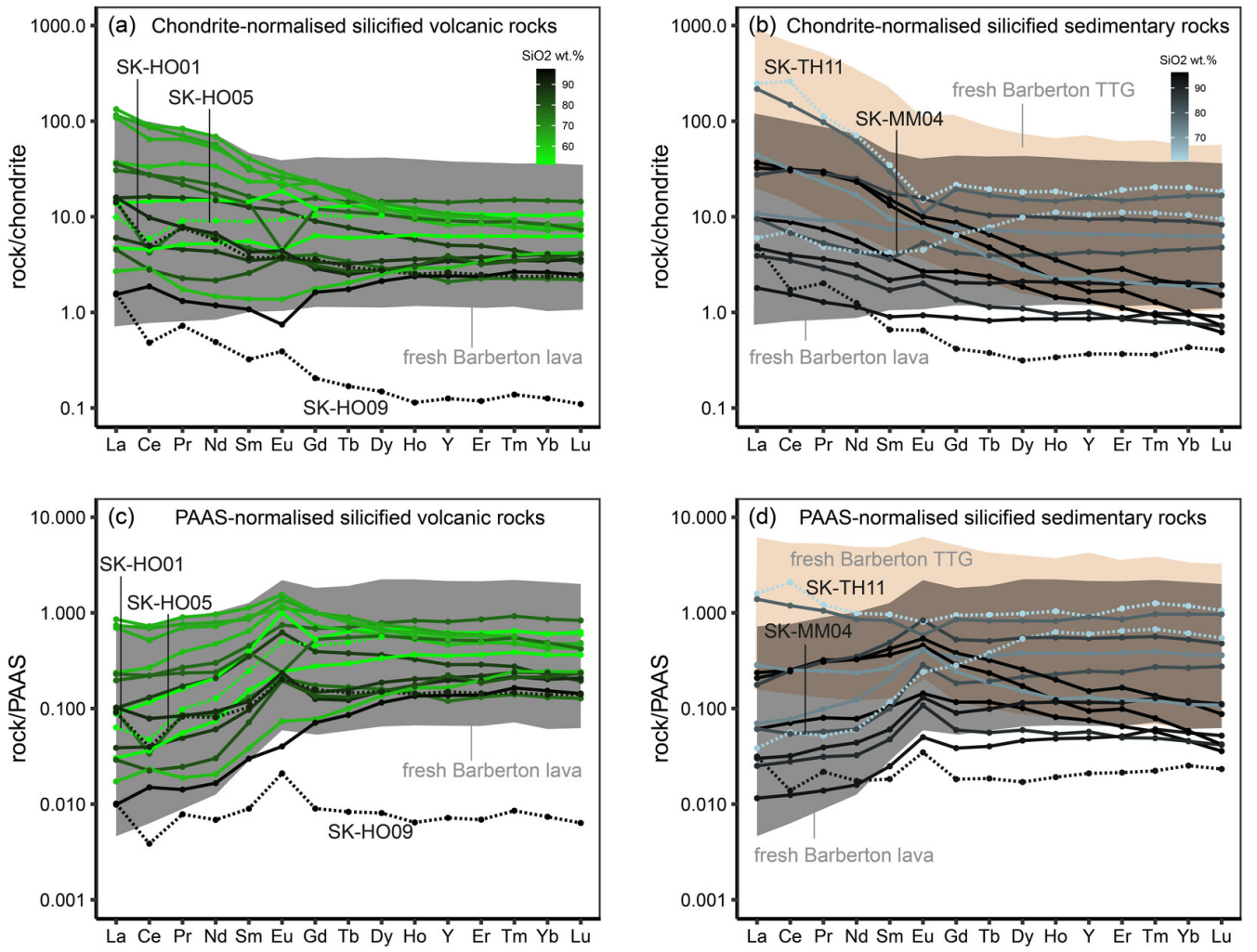

Figure 9. Chondrite (a and b) and PAAS (c and d) normalised REE patterns of the analysed silicified volcanic and sedimentary rock samples. Chondrite values are from Anders and Grevesse (1989), and PAAS values are from Taylor and McLennan (1985). Colour-coding based on SiO_2 concentration illustrates that the REE content of the analysed samples decreases with increasing SiO_2 concentration. For comparison, we report the field of REE patterns measured in fresh Onverwacht volcanic rocks (Chavagnac, 2004; Furnes et al., 2012; Lahaye et al., 1995; Parman et al., 2001; Puchtel et al., 2013; Schneider et al., 2019) and in Barberton granitoids (Moyen et al., 2019). Samples highlighted with dotted lines, including SK-HO01, SK-HO05, SK-HO09, SK-TH11, SK-MM04, exhibit pronounced Ce anomalies discussed in the full text.

various processes that have influenced the composition of silicified volcanic and sedimentary rocks from the Onverwacht Group (BGB) since their deposition on the Paleoarchean seafloor. This is important because geochemical constraints on fluid properties near the Paleoarchean seafloor require excluding the effects of any later process. In this discussion, we corroborate and complement previous studies that have identified a series of processes affecting the mineralogy and the geochemistry of silicified rocks and cherts currently exposed in the Onverwacht Group, including: (1) near-seafloor silicification (Duchac and Hanor, 1987; Hofmann and Harris, 2008), (2) regional metamorphism(s) (Grosch, 2018) and (3) weathering by meteoritic fluids (Bonnand et al., 2020; Lowe and Byerly, 2007b). A summarised geological history of these rocks is illustrated in Figure 11 and the respective influence of each process on their mineralogical and geochemical characteristics is discussed below.

5.1 Evaluating the effects of late-stage weathering and metamorphism

5.1.1 Weathering by post-Archean oxidised fluids and significance of the Ce anomaly

The clay-oxide veinlets crosscutting both quartz veins and microquartz matrix in the analysed rocks indicate the circulation of oxidised fluids after the hydrothermal silicification event (Figures 5, 10d; Lowe and Byerly, 2007b; Reimann et al., 2021; Saitoh et al., 2021). Samples with relatively high volumes of these late-stage clay and oxide phases also exhibit negative Ce anomalies, suggesting that their formation post-dated hydrothermal silicification (Figure 9). In BIFs from the Moodies Group, Bonnand et al. (2020) convincingly attributed similar anomalies to the late-stage addition of LREEs by Ce-free oxidised weathering fluids, based on the La-Ce isotopic system. Consistently, samples

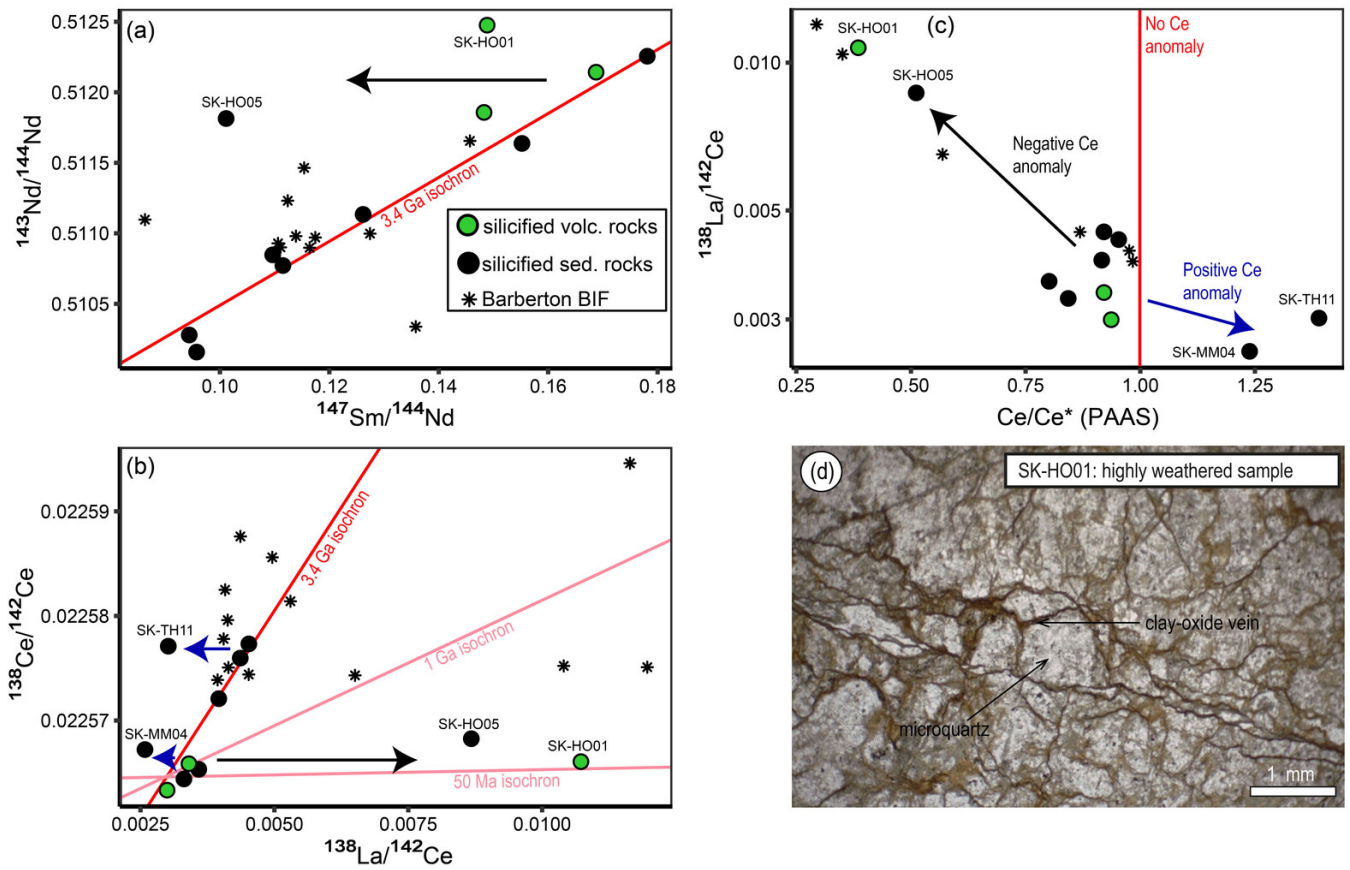

Figure 10. Results for (a) La-Ce and (b) Sm-Nd isotopic systematics measured in selected silicified volcanic and sedimentary rock samples represented in isochron diagrams. (c) $^{138}La/^{142}Ce$ versus Ce/Ce^*_{PAAS}. In (a) and (b) the red oblique lines represent a theoretical isochron of ~3.4 Ga-old material starting from a chondritic isotopic composition, and in (c) shows the position of samples that are free of Ce anomalies. Isochrons of different ages are represented in (b). They are anchored near the current La-Ce isotopic composition of mafic samples that are almost free of Ce anomalies. The alignment of most samples along theoretical isochrons suggests that the parent/daughter ratios of the studied rocks have not been significantly modified by post-Paleoarchean processes. Two samples fall off the regression lines for both isotopic systematics, SK-H005 (chert) and SK-HO01 (volcanic rock sample). These two samples characterised by negative Ce anomalies deviate to the right-hand side of the $^{138}La/^{142}Ce$-$^{138}Ce/^{142}Ce$ regression ($^{138}La/^{142}Ce$ increase). Additionally, samples SK-TH11 and SK-MM04 showing positive Ce anomalies deviate to the left-hand side of the $^{138}La/^{142}Ce$-$^{138}Ce/^{142}Ce$ regression ($^{138}La/^{142}Ce$ decrease). These results prove that the La/Ce fractionation reflected by Ce anomalies is not pristine but reflects post-depositional processes. Panel (d) shows a microphotograph of the highly altered SK-HO01 silicified volcanic rock sample, depicting late-stage veins of clay and oxides. Note that error bars are smaller than the size of symbols. For comparison, isotopic data of Barberton BIF samples from the Fig Tree and Moodies units that were previously published by Hayashi et al. (2004) and Bonnand et al. (2019) are also reported.

in our study displaying negative Ce anomalies deviate from the 3.4 Ga theoretical isochron, following the trend of increasing $^{138}La/^{142}Ce$ ascribed by Bonnand et al. (2020) to oxidising weathering. We thus interpret these negative Ce anomalies as a consequence of weathering in an oxidised environment (Figure 11d). Two samples (SK-TH11 and SK-MM04) displaying positive Ce anomalies likely represent lithologies from where oxidised fluids leached trivalent LREE, leaving behind the immobile Ce^{4+}. Indeed, these samples follow a trend of deceasing $^{138}La/^{142}Ce$, which contrasts with samples featuring negative Ce anomalies (Figure 10b). Silicified volcanic and sedimentary rocks lacking Ce anomalies plot near the theoretical 3.4 Ga La-Ce isochron, indicating that the La-Ce isotopic system remained closed since hydrothermal silicification. This is consistent with the 3.9 ± 0.6 Ga isochron age calculated from the Ce anomaly-free samples regardless of the wide error characterising this age due to the low number and variable nature and origins of samples (Figure S7). The similarity in $^{138}Ce/^{142}Ce$ ratios between non-weathered (i.e. no Ce anomaly) and weathered volcanic rocks demonstrates that the $^{138}La/^{142}Ce$ ratios have been modified during the last 1 Ga (no significant radiogenic ingrowth) as illustrated in Figure 10b. The La-Ce isotopic data clearly demonstrate that the Ce anomalies observed in Paleoarchean silicified volcanic and sedimentary rocks are due to post-Archean circulations of oxidised weathering fluids. Hofmann and Harris (2008) originally proposed this interpretation in their study combining petrographic descriptions and trace ele-

Table 3. Sm-Nd and La-Ce isotope data for selected silicified lavas and sediments. $^{147}Sm/^{144}Nd$ and $^{143}Nd/^{144}Nd$ isotope ratios were measured by MC-ICPMS, Ce isotopes by TIMS and La/Ce ratios by QQQ-ICPMS. *denotes samples that display a positive or negative Ce anomaly. Abbreviations: b=black, g=grey, bw=black-and-white, metased.=metasedimentary. (a) Relative ages (Ma) are based on Armstrong et al. (1990) and Byerly et al. (2019). (b) $^{143}Nd/^{144}Nd$ values were normalised to the isotopic composition of JNdi-1 (0.512099; Garçon et al., 2018) for inter-comparison with other studies. Reported uncertainties are internal precisions (2 SE) in last decimal position. External precisions (2 SD) calculated from repeated standard measurements are 0.50 epsilon unit for Nd and 0.34 for Ce. (c) 2 SD errors on $^{147}Sm/^{144}Nd$ are < 0.25 %. (d) Initial ε_{Ndi} and ε_{Cei} were calculated using the following decay constants: $6.54*10^{-12}$ yr^{-1} for ^{147}Sm α decay to ^{143}Nd, 2.37×10^{-12} yr^{-1} for ^{138}La β^- decay to ^{138}Ce and 4.44×10^{-12} yr^{-1} for ^{138}La β^+ decay to ^{138}Ba. CHUR compositions are taken from Bouvier et al. (2008) and Israel et al. (2020) for Sm-Nd and La-Ce systematics, respectively. (e) 2 SD errors on $^{138}La/^{142}Ce$ are < 0.4 %.

Sample	Latitude	Longitude	Section	Rock	Age(a)	$^{143}Nd/^{144}Nd_{meas}$(b)	$^{147}Sm/^{144}Nd$(c)	ε_{Ndi}(d)	$^{138}Ce/^{142}Ce_{meas}$(b)	$^{138}La/^{142}Ce$(e)	ε_{Cei}(d)
TH11*	-25.9984604	30.8349333	Theespruit	metased. schist	3500	0.510158 (11)	0.0957	-2.96	0.02257710 (18)	0.0030	5.25
TH12	-25.9984604	30.8349333	Theespruit	metased. schist	3500	0.510279 (09)	0.0944	0.03	0.02257732 (23)	0.0045	-0.25
TH14	-25.9984604	30.8349333	Theespruit	metased. schist	3500	0.510771 (09)	0.1115	1.93	0.02257596 (21)	0.0044	-0.26
TH10	-25.9984604	30.8349333	Theespruit	b chert	3500	0.511637 (12)	0.1552	-0.95	0.02257208 (23)	0.0040	-0.48
MM01	-25.9615500	30.8104833	Middle M.	bw chert	3480	0.511134 (08)	0.1262	2.20	0.02256440 (24)	0.0033	-1.46
MM08	-25.9615500	30.8104833	Middle M.	bw chert	3480	0.510847 (33)	0.1096	4.04	0.02256533 (20)	0.0036	-2.08
MM04*	-25.9615500	30.8104833	Middle M.	bw chert	3480	0.512255 (11)	0.1781	0.73	0.02256721 (32)	0.0026	2.48
HO01*	-25.9430878	30.8796744	Hoogg. 3	volcanic rock	3450	0.512475 (08)	0.1488	18.14	0.02256606 (29)	0.0107	-27.93
HO05*	-25.9430878	30.8796744	Hoogg. 3	bw chert	3450	0.511813 (14)	0.1011	26.29	0.02256825 (41)	0.0087	-19.32
HO13	-25.9430878	30.8796744	Hoogg. 3	volcanic rock	3450	0.512142 (09)	0.1688	2.56	0.02256333 (23)	0.0030	-0.78
HO14	-25.9430878	30.8796744	Hoogg. 3	volcanic rock	3450	0.511857 (10)	0.1483	6.10	0.02256586 (22)	0.0034	-1.14
BHVO-2						0.513047 (25)	0.1500		0.02256408 (23)	0.0032	

ment analyses. Our isotopic data provide a robust and unambiguous confirmation.

We also investigate the influence of oxidising weathering fluids on the Sm-Nd isotopic composition of analysed rock samples. Samples displaying significantly negative Ce anomalies (Ce/Ce^*_{PAAS} as low as 0.39–0.51) deviate from the theoretical 3.4 Ga Sm-Nd isochron (Figure 10a). This deviation likely results from a decrease of $^{147}Sm/^{144}Nd$ ratio during the circulation of weathering oxidised fluids (Lahaye et al., 1995). On the other hand, samples that are free of Ce anomalies remain on the theoretical 3.4 Ga Sm-Nd isochron, implying that these samples have preserved their Sm-Nd isotopic systematics ever since their hydrothermal silicification near the Paleoarchean seafloor. The Sm-Nd age of 3.7 ± 1.1 Ga obtained from these samples is within uncertainty consistent with the formation of the Onverwacht Group between 3.5 and 3.0 Ga ago.

Although this study focuses exclusively on silicified volcanic and sedimentary rocks, alteration episodes and prolonged exposure to oxidised meteoric conditions can modify the Ce content of rocks of different compositions (Banerjee et al., 2016; Bonnand et al., 2020; Planavsky et al., 2020; Pfennig et al., 2025). Consequently, Ce anomalies in Archean supracrustal rocks must be interpreted with caution. To evaluate whether a Ce anomaly is pristine or secondary in a rock sample, petrographic screening of meteoric alteration evidence, ideally combined with a detailed study of the La-Ce isotopic system, is strongly recommended. Our study shows that LREE contents can be significantly modified. Hence, future Sm-Nd isotopic studies should consider the absence of a Ce anomaly as a primary criterion for selecting samples likely to preserve isotopic signatures of the Paleoarchean uppermost oceanic crust.

5.1.2 Effects of regional metamorphism on thermometric and geochemical data

Our analyses of chlorite composition and carbonaceous material spectra confirm that a 280–350 °C thermal event re-equilibrated the mineralogy of silicified volcanic and sedimentary rocks across the investigated sections north of the Komati Fault (Figure 6). This finding aligns with previous geothermometric studies in the Onverwacht Group (e.g. Grosch, 2018; Tice et al., 2004; Xie et al., 1997). We agree with prior interpretations that this 280–350 °C temperature range reflects regional metamorphism in the BGB (Figure 11c; Tice et al., 2004; Xie et al., 1997) as it uniformly affects the studied sections despite their age difference. This metamorphic overprint may correspond to one or several metamorphic events previously documented by radiogenic data and which affected the BGB around 3.2, 3.1 or 2.7 Ga (Grosch, 2018; Lécuyer et al., 1994; Stevens and Moyen, 2007; Toulkeridis et al., 1998; Weis and Wasserburg, 1987b).

Because hydrothermal silicification reduced rock permeability (Alleon et al., 2021; Ledevin et al., 2015), important modification of major and trace element compositions of the silicified rocks by pervasive fluid circulation at the metamorphic stage is not expected. The possibility of

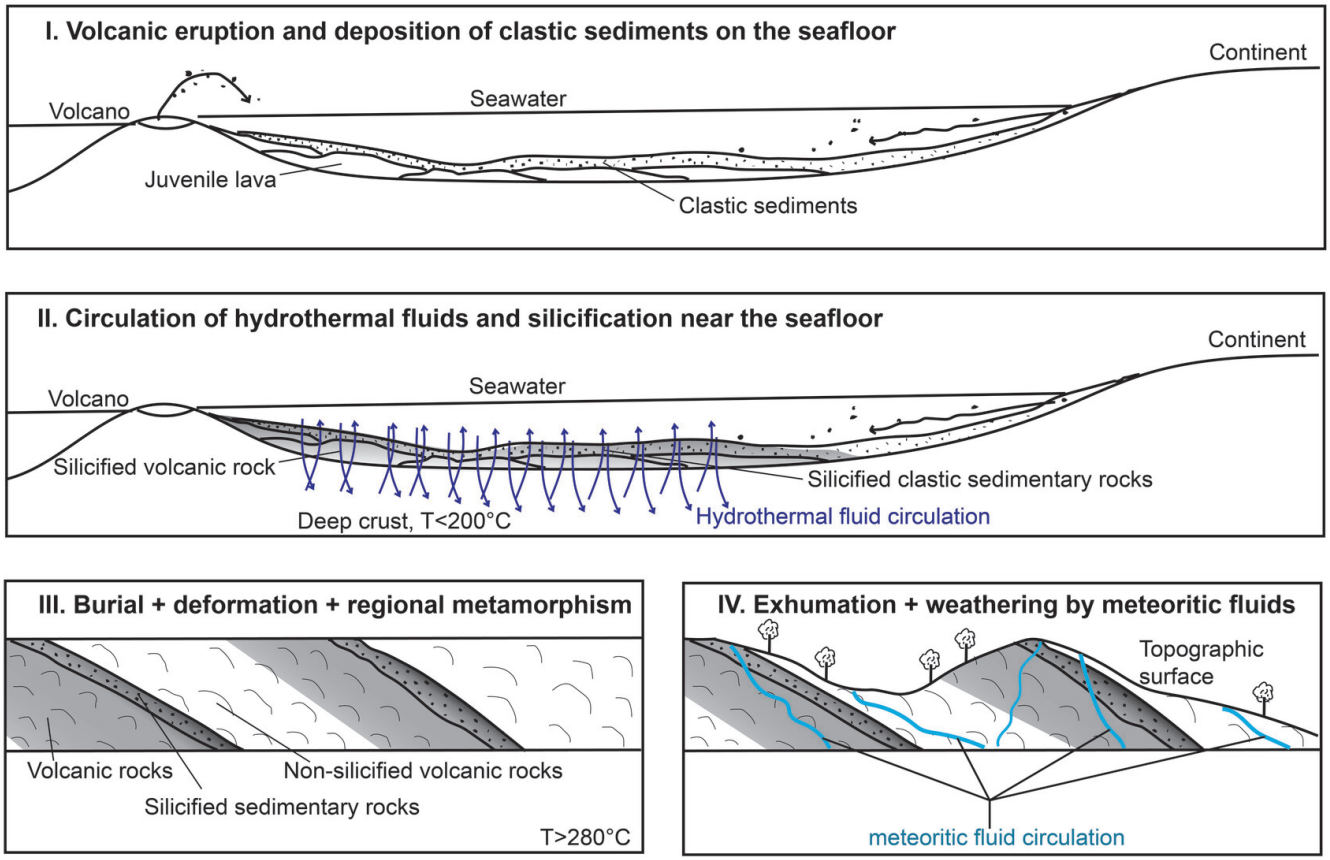

Figure 11. Cartoon illustrating the history of the studied samples reconstructed based on the presented data with a focus on fluid-involving and temperature-involving processes. Stage I represents an episode of submarine volcanism followed by the deposition of continentally derived clastic sediments and/or remobilised pyroclastites. Stage II represents the episode of silicification near the seafloor at < 150 °C due to circulations of seawater-derived hydrothermal fluids that are heated at depth in the oceanic crust (Abraham et al., 2011; de Wit and Furnes, 2016). This episode must have operated in at least two different stages consisting of the silicification of the matrix and the formation of chert veins that crosscut the early silica-rich cement. Stage III represents the regional metamorphism at 280–350 °C that is recorded by the Raman spectra of carbonaceous material and chlorite composition, and that generated variable $\delta^{18}O$ values in quartz-carbonate assemblages. Finally, stage IV illustrates the circulation of meteoritic fluids after exhumation of the studied samples near oxidised meteoric conditions that generated Ce anomalies in some samples. Grey areas represent silicified zones.

focused fluid circulations during regional metamorphism is also precluded by the fact that no generation of veins can be unambiguously related to metamorphism in the silicified rocks. Previous studies have already associated chert or quartz veins like the ones observed in our samples (Figures 3, 5) with hydrothermal silicification near the seafloor (Hofmann and Harris, 2008; Ledevin et al., 2015; Paris et al., 1985) rather than regional metamorphism. Indeed, the similarity of $\delta^{18}O$ and $\delta^{30}Si$ values between quartz veins and microquartz matrix in individual samples suggests that both quartz veins and microquartz precipitated from the same hydrothermal fluid (Kitoga et al., 2024). In this study, maximum $\Delta^{18}O_{quartz\text{-}carbonate}$ obtained in veins collectively provide equilibrium temperatures lower than 280 °C (Figure 7a,b), supporting that these veins did not form during the hotter metamorphic event. We interpret however the notable increase in ankerite $\delta^{18}O$ values in sample SK-MM18, resulting in the quartz-carbonate equilibrium temperatures exceeding the minimum of ~ 110 °C (Figure 7a-c), as an effect of metamorphism, because carbonate is more prone to isotope re-equilibration than quartz (Hyslop et al., 2008). As quartz average $\delta^{18}O$ values do not significantly change in sample SK-MM18, these values are less prone to resetting by metamorphism and are therefore good proxies for reconstructing the composition of Paleoarchean silicifying fluids (e.g. Cammack et al., 2018; Kitoga et al., 2024; Marin-Carbonne et al., 2011; Marin et al., 2010; Stefurak et al., 2015). In the Onverwacht Group, different $\delta^{18}O$ values observed in highly silicified volcanic rocks and cherts (SiO_2 > 90 wt %) from different stratigraphic units (e.g. Komati section versus Mendon 1 section, Figure 7) were ascribed to metamorphism by Knauth and Lowe (2003). However, because quartz, which is the dominant constituent of these rocks, appears to preserve its $\delta^{18}O$ value during regional metamorphism, metamorphism cannot explain the difference of $\delta^{18}O$ in silicified volcanic rocks from different stratigraphic positions in the Onverwacht Group. Instead, we interpreted this observation as due to changes over time in the thermal structure of the crust affecting fluid/rock isotopic exchanges in the sub-

oceanic hydrothermal system (Kitoga et al., 2024; Tatzel et al., 2022). While evidence of alkali (e.g. K_2O, Na_2O and Rb) mobilisation due to metamorphism exists in the literature (e.g. Aguirre, 1988; Tanner and Miller, 1980), such mobilisation cannot explain the highest K_2O/Zr and Rb/Zr (Figure 8e,f) which reflect the presence of fine-grained muscovite in our silicified volcanic and sedimentary rock samples (Figure 4b-f). In fact, K_2O/Zr and Rb/Zr ratios are low in fresh volcanic rocks from the Onverwacht group (Figure 8e,f) that underwent the same metamorphic transformation (Xie et al., 1997) and that are more permeable (Alleon et al., 2021, and therefore more prone to alkali precipitation) than the silicified rocks. Thus, we consider that regional metamorphism operated at low fluid/rock ratio and cannot have significantly affected the bulk-rock composition of the analysed rocks. We agree with Lécuyer et al. (1994) that geochemical features such as alkali, REE and HFSE abundances discussed below were not significantly modified at the metamorphic stage.

5.2 Quantifying the temperature of the Paleoarchean silicifying hydrothermal fluids

We determined a minimum equilibrium temperature of $\sim 110 \pm 50$ °C from the maximum $\Delta^{18}O_{quartz\text{-}carbonate}$ obtained in our dataset from silicified volcanic rock sample SK-ME18. This temperature is the lowest so far obtained quantitatively for Archean hydrothermal fluids using oxygen isotope fractionation between quartz and carbonate in silicified rock and chert samples from the BGB (Figure 7). Sample SK-MM18 exhibits no Ce anomaly or clay-oxide veins, which would be expected if its recorded temperature resulted from alteration by late-stage weathering fluids (Section 5.1.1). Thus, we interpret this temperature as the closest estimate of the hydrothermal fluid temperature responsible for silicification. This temperature is significantly lower than equilibrium temperatures of 148 to 310 °C derived from both maximum and mean $\Delta^{18}O_{quartz\text{-}carbonate}$ of all other quartz-carbonate assemblages analysed in this study (Figure 7). It is also lower than temperatures of 186 to 301 °C reported by Marin-Carbonne et al. (2011) who were the first to apply this thermometer on Onverwacht cherts. This suggests that the SK-MM18 sample presents a rare, well-preserved quartz-carbonate assemblage, providing a unique opportunity to constrain the temperature of hydrothermal fluids from which quartz and carbonate initially co-precipitated.

The $\Delta^{18}O_{quartz\text{-}carbonate}$ thermometer is more reliable than those based on $\delta^{18}O$ or $\delta^{30}Si$ values of quartz or carbonate individually because the latter thermometers imply an assumption about the $\delta^{18}O$ value of silicifying fluids (Abraham et al., 2011; Hofmann and Harris, 2008; Shibuya et al., 2012; Tatzel et al., 2024). Most previous studies proposed that Paleoarchean silicifying fluids must have been cooler than 150 °C based on bulk-rock $\delta^{18}O$ or $\delta^{30}Si$ values of silicified volcanic rocks, in agreement with the temperature of ~ 110 °C obtained here (e.g. Abraham et al., 2011; Hofmann and Harris, 2008). However, these studies relied on the assumption that the Si and O isotopic composition of Archean fluids was similar to that of modern seawater, which is not necessarily accurate (Bindeman and O'Neil, 2022; Jaffrés et al., 2007; Kitoga et al., 2024). We acknowledge that the temperature of ~ 110 °C constrained here for the silicifying hydrothermal fluids has the drawback of deriving from a single quartz-carbonate assemblage. Yet, it represents a precious quantitative temperature with no assumption on the composition of hydrothermal fluids. Although this calculated temperature may include uncertainties due to thermometer calibration and carbonate type (Chacko and Deines, 2008; Marin-Carbonne et al., 2011), these parameters are unlikely to affect it beyond the estimated uncertainty of ± 50 °C. The relatively low temperature estimated here is consistent with the sequestration of alkalis (e.g. high K_2O/Zr and Rb/Zr in Figure 8e,f), which is also a classical characteristic of volcanic rocks undergoing low-temperature (< 150 °C) hydrothermal alteration near the modern seafloor (Alt et al., 2010; Bach et al., 2003; Coogan and Gillis, 2018; Gillis and Robinson, 1990; Hart and Staudigel, 1982; Hauff et al., 2003; Kelley et al., 2003).

The possibility that metamorphism may have increased the $\delta^{18}O$ value of carbonate even in the best-preserved assemblage yielding a temperature of ~ 110 °C, albeit to lesser extent than it did for the other analysed assemblages (Section 5.1.2, Figure 7), cannot be completely ruled out. Therefore, the temperature of ~ 110 °C constrained here may represent only an upper limit for the real temperature of the silicifying hydrothermal fluid.

5.3 Inferences on geochemical signatures related to hydrothermal silicification near the Paleoarchean seafloor

5.3.1 Evidence that seawater-like Y/Ho and Zr/Hf ratios could not derive from hydrothermal silicification

Both cherts precipitated chemically from seawater and cherts resulting from hydrothermal silicification of clastic sediments are present in Paleoarchean terrains in general (Allwood et al., 2010; Djokic et al., 2024; van den Boorn et al., 2010), and particularly in the BGB (Ledevin et al., 2014, 2019; Lowe and Byerly, 2007a; Tice and Lowe, 2006). These different types of rocks equilibrated with very different types of fluids, namely seawater for chemical cherts and hydrothermal fluid for the silicified clastic sedimentary rocks (Kitoga et al., 2024; Lowe et al., 2020). Distinguishing these different types of rocks (or cherts) is therefore essential for constraining separately the properties of the Paleoarchean seawater and hydrothermal fluids (Lowe et al., 2020; Perry and Lefticariu, 2007).

We have observed sedimentary grain contours and erosive bases in grey and black-and-white chert samples (Figures 4d, 5), which we therefore classify as silicified clastic sedimentary rocks. In cases where petrographic observations do not allow a conclusive distinction between the different types of cherts, geochemical criteria provide the only possible way to determine the chert type (e.g. Bolhar et al., 2004; Brengman and Fedo, 2018). Cherts displaying elevated Y/Ho or Zr/Hf ratios are generally considered as pure seawater precipitates

(Allwood et al., 2010; Djokic et al., 2024; Geilert et al., 2014; Sugahara et al., 2010; van den Boorn et al., 2007), because Phanerozoic oceans and their precipitated chemical sediments show high Y/Ho and Zr/Hf ratios (Alibo and Nozaki, 1999; Hongo et al., 2006; Olivier and Boyet, 2006; Schmidt et al., 2014). However, this classification has been challenged by studies suggesting that hydrothermally silicified volcanic and clastic sedimentary rocks can also acquire high Y/Ho and Zr/Hf ratios through water-rock interactions (Brengman and Fedo, 2018; Yoshida et al., 2024). Although our trace element data demonstrate that the concentration of REEs was modified during the hydrothermal silicification of volcanic and sedimentary rocks (see Section 5.1.1), these data combined with a literature compilation reveal that the Y/Ho and Zr/Hf ratios (Figure 8a,b) of silicified volcanic rocks remained within the field of fresh volcanic rocks from the Onverwacht Group. This demonstrates that hydrothermal silicification did not increase Y/Ho and Zr/Hf ratios to extreme values characteristic of the modern ocean and its chemically precipitated sediments, consistently with the proposition of Allwood et al. (2010), Geilert et al. (2014) and van den Boorn et al. (2010). Importantly, even black cherts lacking clear petrographic textures of clastic sedimentary rocks also exhibit Y/Ho and Zr/Hf ratios within the range of fresh volcanic rocks. This shows that the black cherts studied here originated from the silicification of clastic sedimentary units and are not pure seawater precipitates.

Cherts with high Y/Ho and Zr/Hf (up to 124 and 103, respectively) have been identified in the Buck Reef Unit of the Onverwacht Group (see the highest values on Figure 8a,b; Geilert et al., 2014; Ledevin et al., 2019). As per petrographic descriptions in previous studies, these cherts have a pure white or black colour and are free of clast ghosts observed in some of our silicified clastic sedimentary rock samples (Figure 5), which is the reason why they were interpreted as pure seawater precipitates (Geilert et al., 2014; Ledevin et al., 2019; Lowe et al., 2020). Indeed, the elevated Y/Ho and Zr/Hf ratios observed in some Buck Reef Unit cherts are absent in silicified volcanic and sedimentary rocks, confirming that these values are inherited from seawater. Stable O and Si isotopic analyses also confirmed the presence of seawater-derived silica in these seawater-precipitated cherts (Kitoga et al., 2024; Lowe et al., 2020; Marin-Carbonne et al., 2011; Stefurak et al., 2015). Additionally, the triple oxygen isotopic composition of these chemical cherts demonstrated that part of their oxygen originated from hydrothermal overprint on the seafloor (Kitoga et al., 2024). Thus, their current Y/Ho and Zr/Hf ratios may not necessarily represent the real values that they featured directly after precipitation from the Paleoarchean seawater. Yet, we maintain that the elevated Y/Ho and Zr/Hf values are undisputable evidence that these cherts precipitated chemically from seawater before eventually interacting with hydrothermal fluids on the seafloor. Such elevated Y/Ho and Zr/Hf ratios are rare in Barberton cherts (Figure 8a,b), highlighting the scarcity of reliable proxies of pure Archean seawater in this terrain (e.g. Lowe et al., 2020). Investigations of seawater properties in the BGB should focus on stratigraphic units such as the Buck Reef Unit showing potential trace element signatures of pure (or only minimally modified) seawater-precipitated cherts.

5.3.2 *Evidence and significance of differential REE mobilisation during hydrothermal silicification*

The composition of silicified volcanic and sedimentary rocks unaffected by late-stage weathering (i.e. those exhibiting minimal or no Ce anomaly, see Figure 9) supports the previous interpretation that Paleoarchean hydrothermal silicification altered REE concentrations and ratios (Brengman and Fedo, 2018; Hofmann and Harris, 2008). Abundance of REEs systematically decreases with increasing SiO_2 content (Figure 9), consistent with dilution by the addition of silica phases precipitated from hydrothermal fluids into the rocks. Both positive and negative Eu anomalies are also observed in chondrite-normalised REE patterns of the silicified volcanic and sedimentary rock samples (Figure 9a,b). As proposed in earlier studies (Bach et al., 2003; Hofmann and Harris, 2008; Yoshida et al., 2024), these Eu anomalies are attributed to (1) plagioclase dissolution and (2) the decoupled charge-dependent behaviour of Eu^{2+} relative to REE^{3+} in aqueous systems. A decrease of the Sm/Nd ratio with increasing SiO_2 content is also observed in silicified volcanic and sedimentary rocks (Figure 8c). Although the bulk-rock Sm/Nd ratio is expected to decrease with increasing SiO_2 content due to magmatic differentiation (Villemant, 1988; Garçon, 2021; Bea et al., 2023), this process does not explain our observation because the increase of SiO_2 in these rocks is mainly due to replacement of primary minerals by hydrothermal microquartz (Figure 4). Instead, the decrease of Sm/Nd with increasing SiO_2 can be explained by the two-stage model of fluid-rock interaction in early Archean silica-rich hydrothermal systems proposed by Kutyrev et al. (2024). According to this model, dissolution of primary magmatic phases (e.g. glass and plagioclase) firstly allowed the release of elements (including REEs) from the rocks by a (relatively acidic) fluid, then, in a second stage, these elements were selectively re-precipitated into the rocks within or at the interface of secondary mineral phases such as oxhydroxide, clay and microquartz. The Archean seawater and resultant silica-rich hydrothermal fluid are generally believed to have been acidic (Halevy and Bachan, 2018; Krissansen-Totton et al., 2018; Rouchon and Orberger, 2008), and lighter REEs are known to preferentially re-precipitate from such acidic fluids compared to heavier REEs (Calvert et al., 1987; Falcone et al., 2022; Quinn et al., 2006). The decrease of Sm/Nd ratio with increasing SiO_2 concentration may therefore reflect the acidic conditions of the hydrothermal fluids.

Silicified volcanic and sedimentary rocks also exhibit a wider range of Lu/Hf ratio compared to fresh volcanic rocks from the Onverwacht Group. Unlike the systematic decrease in Sm/Nd ratios, the variable Lu/Hf values cannot be fully explained by dissolution-precipitation reactions during interaction with acidic hydrothermal fluids (Figure 8d). Although no data exists on the relative stability of Lu and Hf in

acidic hydrothermal fluids, the continuous evolution of most silicified volcanic and sedimentary rocks towards lower Lu/Hf ratios with increasing SiO_2 content (Figure 8d) supports that the circulation of acidic hydrothermal fluids promoted the development of lower Lu/Hf ratios relative to fresh volcanic rocks (André et al., 2019). However, this mechanism cannot explain the highest Lu/Hf ratios observed in some silicified samples (Figure 8d). We tentatively propose that the highest Lu/Hf ratios resulted from the late-stage precipitation of carbonate minerals after hydrothermal fluids evolved toward a more alkaline composition. Sedimentation or eruption on the seafloor could isolate the originally acidic hydrothermal fluids from recharge of Paleoarchean seawater, allowing these fluids to evolve towards a more alkaline composition at an advanced stage of silicification (Shibuya et al., 2010). Modern hydrothermal systems show that, in alkaline fluids, HFSE and HREEs behave differently: HFSE tend to remain as free aqueous metals, whereas HREEs preferentially form stable carbonate complexes ($REECO^{3-}$; Calvert et al., 1987; Falcone et al., 2022; Quinn et al., 2006). Thus, carbonate precipitation in this context would increase the Lu/Hf ratio of the rock. In our sample set, the highest Lu/Hf ratios are associated with highly silicified rocks (SiO_2 > 80 wt %; Figure 8d) and a greater abundance of carbonate phases (e.g. carbonates shown in Figure 7e-h), supporting the hypothesis of late-stage carbonate precipitation. Collectively, these observations demonstrate that fluid-rock interactions led to differential mobilisation and redistribution of REEs and HFSE, significantly modifying Sm/Nd and Lu/Hf ratios of the rock, although the precise link between these chemical signatures and fluid pH evolution warrants further mineralogical analyses.

The modification of Sm/Nd and Lu/Hf ratios due to hydrothermal silicification of the uppermost portion of the Paleoarchean oceanic crust implies that the composition of hydrothermal fluids discharged into Archean oceans was different from that of the leached oceanic crust. Consequently, chemical fractionation of Lu/Hf during hydrothermal processes could be considered as an alternative option to explain the highly radiogenic Hf isotopic signature observed in Archean BIF commonly interpreted to result from incongruent weathering of felsic continents (e.g. Viehmann et al., 2018, 2020). Additionally, given the significant modification of Sm/Nd and Lu/Hf ratios by hydrothermal silicification, silicified volcanic and sedimentary rocks would have developed, over time, less radiogenic ε_{Nd} and more variable ε_{Hf} values compared to fresh Paleoarchean mafic-ultramafic volcanic rocks. The potential recycling of a silicified uppermost oceanic crust, chemically distinct from non-silicified crust (e.g André et al., 2019; Deng et al., 2019; Kitoga et al., 2024; Lei et al., 2023; Trail et al., 2018; Vezinet et al., 2018) must therefore be considered when interpreting Nd and Hf isotopic compositions to study early Earth crustal evolution. Evidence of recycled material with lower ε_{Nd} and ε_{Hf} compared to pristine Archean mafic crust can no longer be unambiguously linked to the existence of felsic continents on the early Earth (Dhuime et al., 2012; Roberts and Santosh, 2018), as such isotopic signatures could equally record the recycling of a silicified oceanic crust.

6 Concluding remarks

The comprehensive dataset acquired in this study allows identification of incremental petro-geochemical modifications recorded by seafloor-derived, hydrothermally silicified volcanic and clastic sedimentary rocks from the 3.5–3.2 Ga-old Onverwacht Group throughout their long geological history. This allows us to better constrain the geochemical signatures inherited from hydrothermal silicification near the Archean seafloor. Late-stage clay and Fe-oxide phases associated with bulk-rock Ce anomalies document weathering of some of the analysed rocks by oxidised fluids. Using the La-Ce radiometric system, we demonstrate that this weathering episode operated during the last 1 Ga, because $^{138}Ce/^{142}Ce$ ratios are not considerably different between weathered samples displaying Ce anomalies and non-weathered samples. This event is quite recent compared to the Paleoarchean age of the analysed rocks.

In addition, an episode of regional metamorphism constrained by chlorite thermometry and Raman spectroscopy of carbonaceous materials appears to have recrystallised the silicified volcanic and sedimentary rocks at temperatures that exceeded 280 °C. Lacking textural and geochemical evidence of elevated fluid/rock ratio for this metamorphic episode, we consider that metamorphism did not significantly modify the bulk-rock composition of the analysed rocks. Although an evident influence of late-stage regional metamorphism on the $\delta^{18}O$ value of carbonate is observed, the $\Delta^{18}O_{quartz\text{-}carbonate}$ of a uniquely preserved quartz-carbonate assemblage allows us to quantify an equilibrium temperature of 110 ± 50 °C, which is interpreted as the upper limit of the silicifying hydrothermal fluid temperature.

After excluding samples affected by post-Archean weathering (Ce anomalies), our results demonstrate that hydrothermal silicification could not produce supra-chondritic Y/Ho and Zr/Hf ratios characterising Archean seawater-precipitated chemical cherts. Thus, these elemental ratios remain robust indicators that distinguish seawater-precipitated cherts from hydrothermally silicified clastic sedimentary rocks. Furthermore, silicification is shown to have lowered Sm/Nd ratios and produced wide variations of Lu/Hf ratios in silicified volcanic and clastic sedimentary rocks. Consequently, silicified Paleoarchean volcanic and clastic sedimentary rocks could evolve towards distinct radiogenic Nd and Hf isotopic signatures relative to their non-silicified counterparts. The effect of hydrothermal silicification must be considered more carefully in future Sm-Nd and Lu-Hf isotope studies of Archean rocks.

Acknowledgments

The results presented in this study are part of L.S. Kitoga's PhD research that was funded by the French Centre National de la Recherche Scientifique. Data acquisitions were supported by the BUCOMO collaborative project of J-F Moyen

and G. Stevens as well as the ISOREE ERC grant of M. Boyet (grant agreement n° 682778). We thank the different individuals who provided invaluable assistance during our analytical sessions at University Clermont Auvergne (K. Surchowsky, M. Neimard, M. Gannoun, D. Auclair, C. Bosq and F. Schiavi), Stellenbosch University (A. Herschel, M. Frazenburg and M. Grobbellar) and Lausanne University, especially the SwissSIMS team (T. Bovay and A.S. Bouvier). We also thank D. Zakharov and Q. Aquila for discussions on seawater-crust interactions during the Archean Eon, and P. Lanari for discussion on chlorite thermometry. This manuscript benefited of careful editorial handling and comments from Professors Ramananda Chakrabarti and James Darling, and constructive recommendations from Dr. Alex McCoy-West and an anonymous reviewer during the peer-review stage. This is contribution N° 740 of the ClerVolc program of the International Research Center for Disaster Sciences and Sustainable Development of the University of Clermont Auvergne.

Data, code, and outputs availability

All the data acquired on analysed samples and reference materials, together with Supporting Figures and the previously published data compiled for comparison with our results, are accessible in OPGC repository (Kitoga et al., 2025, https://doi.org/10.25519/QXR1-9Y88). Main text figures and tables are available for download in the online version of this article.

Competing interests

The authors declare no competing interests.

Licence agreement

References

Abraham K, Hofmann A, Foley S, Cardinal D, Harris C, Barth M, André L (2011). Coupled silicon–oxygen isotope fractionation traces Archaean silicification. *Earth and Planetary Science Letters* 301(1–2): 222–230. doi:10.1016/j.epsl.2010.11.002.

Aguirre L (1988). Chemical mobility during low-grade metamorphism of a Jurassic lava flow: Río Grande Formation, Peru. *Journal of South American Earth Sciences* 1(4): 343–361. doi:10.1016/0895-9811(88)90022-3.

Alibo DS, Nozaki Y (1999). Rare earth elements in seawater: particle association, shale-normalization, and Ce oxidation. *Geochimica et Cosmochimica Acta* 63(3–4): 363–372. doi:10.1016/s0016-7037(98)00279-8.

Alleon J, Bernard S, Olivier N, Thomazo C, Marin-Carbonne J (2021). Inherited geochemical diversity of 3.4 Ga organic films from the Buck Reef Chert, South Africa. *Communications Earth and Environment* 2(1): 4–10. doi:10.1038/s43247-020-00066-7.

Allwood AC, Kamber BS, Walter MR, Burch IW, Kanik I (2010). Trace elements record depositional history of an Early Archean stromatolitic carbonate platform. *Chemical Geology* 270(1–4): 148–163. doi:10.1016/j.chemgeo.2009.11.013.

Alt JC, Laverne C, Coggon RM, Teagle DAH, Banerjee NR, Morgan S, Smith-Duque CE, Harris M, Galli L (2010). Subsurface structure of a submarine hydrothermal system in ocean crust formed at the East Pacific Rise, ODP/IODP Site 1256. *Geochemistry, Geophysics, Geosystems* 11(10): 1–28. doi:10.1029/2010gc003144.

Anders E, Grevesse N (1989). Abundances of the elements: Meteoritic and solar. *Geochimica et Cosmochimica Acta* 53(1): 197–214. doi:10.1016/0016-7037(89)90286-x.

André L, Abraham K, Hofmann A, Monin L, Kleinhanns IC, Foley S (2019). Early continental crust generated by reworking of basalts variably silicified by seawater. *Nature Geoscience* 12(9): 769–773. doi:10.1038/s41561-019-0408-5.

André L, Monin L, Hofmann A (2022). The origin of early continental crust: New clues from coupling Ge/Si ratios with silicon isotopes. *Earth and Planetary Science Letters* 582: 117415. doi:10.1016/j.epsl.2022.117415.

Anhaeusser CR (1981). *Chapter 6 Geotectonic Evolution of the Archaean Successions in the Barberton Mountain Land, South Africa*, vol. 4, p. 137–160. Elsevier. doi:10.1016/s0166-2635(08)70011-2.

Armstrong R, Compston W, de Wit M, Williams I (1990). The stratigraphy of the 3.5-3.2 Ga Barberton Greenstone Belt revisited: A single zircon ion microprobe study. *Earth and Planetary Science Letters* 101(1): 90–106. doi:10.1016/0012-821x(90)90127-j.

Bach W, Peucker-Ehrenbrink B, Hart SR, Blusztajn JS (2003). Geochemistry of hydrothermally altered oceanic crust: DSDP/ODP Hole 504B – Implications for seawater-crust exchange budgets and Sr- and Pb-isotopic evolution of the mantle. *Geochemistry, Geophysics, Geosystems* 4(3): 40–55. doi:10.1029/2002gc000419.

Banerjee A, Chakrabarti R, Mandal S (2016). Geochemical anatomy of a spheroidally weathered diabase. *Chemical Geology* 440: 124–138. doi:10.1016/j.chemgeo.2016.07.008.

Bau M (1996). Controls on the fractionation of isovalent trace elements in magmatic and aqueous systems: evidence from Y/Ho, Zr/Hf, and lanthanide tetrad effect. *Contributions to Mineralogy and Petrology* 123(3): 323–333. doi:10.1007/s004100050159.

Bea F, Montero P, Barcos L, Cambeses A, Molina JF, Morales I (2023). Understanding Nd model ages of granite rocks: The effects of the 147Sm/144Nd variability during partial melting and crystallization. *Lithos* 436–437: 106940. doi:10.1016/j.lithos.2022.106940.

Beyssac O, Goffé B, Chopin C, Rouzaud JN (2002). Raman spectra of carbonaceous material in metasediments: a new geothermometer. *Journal of Metamorphic Geology* 20(9): 859–871. doi:10.1046/j.1525-1314.2002.00408.x.

Bindeman I, O'Neil J (2022). Earth's earliest hydrosphere recorded by the oldest hydrothermally-altered oceanic crust: Triple oxygen and hydrogen isotopes in the 4.3-3.8 Ga Nuvvuagittuq belt, Canada. *Earth and Planetary Science Letters* 586: 117539. doi:10.1016/j.epsl.2022.117539.

Bolhar R, Kamber BS, Moorbath S, Fedo CM, Whitehouse MJ (2004). Characterisation of early Archaean chemical sediments by trace element signatures. *Earth and Planetary Science Letters* 222(1): 43–60. doi:10.1016/j.epsl.2004.02.016.

Bonnand P, Israel C, Boyet M, Doucelance R, Auclair D (2019). Radiogenic and stable Ce isotope measurements by thermal ionisation mass spectrometry. *Journal of Analytical Atomic Spectrometry* 34(3): 504–516. doi:10.1039/c8ja00362a.

Bonnand P, Lalonde S, Boyet M, Heubeck C, Homann M, Nonnotte P, Foster I, Konhauser K, Köhler I (2020). Post-depositional REE mobility in a Paleoarchean banded iron formation revealed by La-Ce geochronology: A cautionary tale for signals of ancient oxygenation. *Earth and Planetary Science Letters* 547: 116452. doi:10.1016/j.epsl.2020.116452.

van den Boorn S, van Bergen M, Vroon P, de Vries S, Nijman W (2010). Silicon isotope and trace element constraints on the origin of ∼3.5 Ga cherts: Implications for Early Archaean marine environments. *Geochimica et Cosmochimica Acta* 74(3): 1077–1103. doi:10.1016/j.gca.2009.09.009.

van den Boorn SH, van Bergen MJ, Nijman W, Vroon PZ (2007). Dual role of seawater and hydrothermal fluids in Early Archean chert formation: Evidence from silicon isotopes. *Geology* 35(10): 939–942. doi:10.1130/g24096a.1.

Bourdelle F (2021). Low-Temperature Chlorite Geothermometry and Related Recent Analytical Advances: A Review. *Minerals* 11(2): 130. doi:10.3390/min11020130.

Bouvier A, Vervoort JD, Patchett PJ (2008). The Lu–Hf and Sm–Nd isotopic composition of CHUR: Constraints from unequilibrated chondrites and implications for the bulk composition of terrestrial planets. *Earth and Planetary Science Letters* 273(1–2): 48–57. doi:10.1016/j.epsl.2008.06.010.

Brengman LA, Fedo CM (2018). Development of a mixed seawater-hydrothermal fluid geochemical signature during alteration of volcanic rocks in the Archean (∼2.7 Ga) Abitibi Greenstone Belt, Canada. *Geochimica et Cosmochimica Acta* 227: 227–245. doi:10.1016/j.gca.2018.02.019.

Byerly GR, Lowe DR, Heubeck C (2019). *Geologic Evolution of the Barberton Greenstone Belt—A Unique Record of Crustal Development, Surface Processes, and Early Life 3.55–3.20 Ga*, p. 569–613. Elsevier. doi:10.1016/b978-0-444-63901-1.00024-1.

Bégué F, Baumgartner LP, Bouvier AS, Robyr M (2019). Reactive fluid infiltration along fractures: Textural observations coupled to in-situ isotopic analyses. *Earth and Planetary Science Letters* 519: 264–273. doi:10.1016/j.epsl.2019.05.024.

Calvert S, Piper D, Baedecker P (1987). Geochemistry of the rare earth elements in ferromanganese nodules from DOMES Site A, northern equatorial Pacific. *Geochimica et Cosmochimica Acta* 51(9): 2331–2338. doi:10.1016/0016-7037(87)90287-0.

Cammack J, Spicuzza M, Cavosie A, Van Kranendonk M, Hickman A, Kozdon R, Orland I, Kitajima K, Valley J (2018). SIMS microanalysis of the Strelley Pool Formation cherts and the implications for the secular-temporal oxygen-isotope trend of cherts. *Precambrian Research* 304: 125–139. doi:10.1016/j.precamres.2017.11.005.

Chacko T, Deines P (2008). Theoretical calculation of oxygen isotope fractionation factors in carbonate systems. *Geochimica et Cosmochimica Acta* 72(15): 3642–3660. doi:10.1016/j.gca.2008.06.001.

Chavagnac V (2004). A geochemical and Nd isotopic study of Barberton komatiites (South Africa): implication for the Archean mantle. *Lithos* 75(3–4): 253–281. doi:10.1016/j.lithos.2004.03.001.

Clayton RN, O'Neil JR, Mayeda TK (1972). Oxygen isotope exchange between quartz and water. *Journal of Geophysical Research* 77(17): 3057–3067. doi:10.1029/jb077i017p03057.

Condie KC, Viljoen MJ, Kable EJD (1977). Effects of alteration on element distributions in archean tholeiites from the Barberton greenstone belt, South Africa. *Contributions to Mineralogy and Petrology* 64(1): 75–89. doi:10.1007/bf00375286.

Coogan L, Gillis K (2018). Temperature dependence of chemical exchange during seafloor weathering: Insights from the Troodos ophiolite. *Geochimica et Cosmochimica Acta* 243: 24–41. doi:10.1016/j.gca.2018.09.025.

Cutts K, Stevens G, Hoffmann J, Buick I, Frei D, Münker C (2014). Paleo- to Mesoarchean polymetamorphism in the Barberton Granite-Greenstone Belt, South Africa: Constraints from U-Pb monazite and Lu-Hf garnet geochronology on the tectonic processes that shaped the belt. *Geological Society of America Bulletin* 126(3–4): 251–270. doi:10.1130/b30807.1.

Cutts KA, Stevens G, Kisters A (2015). Reply to "Paleo- to Mesoarchean polymetamorphism in the Barberton granite-greenstone belt, South Africa: Constraints from U-Pb monazite and Lu-Hf garnet geochronology on the tectonic processes that shaped the belt: Discussion" by M. Brown. *Geological Society of America Bulletin* 127(11–12): 1558–1563. doi:10.1130/b31304.1.

Decker NB, Byerly GR, Thompson Stiegler M, Lowe DR, Stefurak E (2015). High resolution tephra and U/Pb chronology of the 3.33–3.26 Ga Mendon Formation, Barberton Greenstone Belt, South Africa. *Precambrian Research* 261: 54–74. doi:10.1016/j.precamres.2015.02.003.

Deng Z, Chaussidon M, Guitreau M, Puchtel IS, Dauphas N, Moynier F (2019). An oceanic subduction origin for Archaean granitoids revealed by silicon isotopes. *Nature Geoscience* 12(9): 774–778. doi:10.1038/s41561-019-0407-6.

Dhuime B, Hawkesworth CJ, Cawood PA, Storey CD (2012). A Change in the Geodynamics of Continental Growth 3 Billion Years Ago. *Science* 335(6074): 1334–1336. doi:10.1126/science.1216066.

Diener JF, Stevens G, Kisters AF, Poujol M (2005). Metamorphism and exhumation of the basal parts of the Barberton greenstone belt, South Africa: Constraining the rates of Mesoarchaean tectonism. *Precambrian Research* 143(1–4): 87–112. doi:10.1016/j.precamres.2005.10.001.

Djokic T, Bolhar R, Brengman L, Havig J, Van Kranendonk M (2024). Trace elements (REE + Y) reveal marine, subaerial, and hydrothermal controls on an early Archean habitat for life: The 3.48Ga volcanic-caldera system of the dresser formation, Pilbara Craton. *Chemical Geology* 644: 121865. doi:10.1016/j.chemgeo.2023.121865.

Drabon N, Lowe DR (2021). Progressive accretion recorded in sedimentary rocks of the 3.28–3.23 Ga Fig Tree Group, Barberton Greenstone Belt. *GSA Bulletin* 134(5–6): 1258–1276. doi:10.1130/b35973.1.

Duchac KC, Hanor JS (1987). Origin and timing of the metasomatic silicification of an early archean komatiite sequence, barberton mountain land, South Africa. *Precambrian Research* 37(2): 125–146. doi:10.1016/0301-9268(87)90075-1.

Dziggel A, Stevens G, Poujol M, Anhaeusser C, Armstrong R (2002). Metamorphism of the granite–greenstone terrane south of the Barberton greenstone belt, South Africa: an insight into the tectono-thermal evolution of the 'lower' portions of the Onverwacht Group. *Precambrian Research* 114(3–4): 221–247. doi:10.1016/s0301-9268(01)00225-x.

Falcone E, Federico C, Boudoire G (2022). Geochemistry of trace metals and Rare Earth Elements in shallow marine water affected by hydrothermal fluids at Vulcano (Aeolian Islands, Italy). *Chemical Geology* 593: 120756. doi:10.1016/j.chemgeo.2022.120756.

Furnes H, Robins B, de Wit M (2012). Geochemistry and petrology of lavas in the Upper Onverwacht Suite, Barberton Mountain Land, South Africa. *South African Journal of Geology* 115(2): 171–210. doi:10.2113/gssajg.115.2.171.

Garçon M (2021). Episodic growth of felsic continents in the past 3.7 Ga. *Science Advances* 7(39). doi:10.1126/sciadv.abj1807.

Garçon M, Boyet M, Carlson RW, Horan MF, Auclair D, Mock TD (2018). Factors influencing the precision and accuracy of Nd isotope measurements by thermal ionization mass spectrometry. *Chemical Geology* 476: 493–514. doi:10.1016/j.chemgeo.2017.12.003.

Geilert S, Vroon PZ, van Bergen MJ (2014). Silicon isotopes and trace elements in chert record early Archean basin evolution. *Chemical Geology* 386: 133–142. doi:10.1016/j.chemgeo.2014.07.027.

Gillis KM, Robinson PT (1990). Patterns and processes of alteration in the lavas and dykes of the Troodos Ophiolite, Cyprus. *Journal of Geophysical Research: Solid Earth* 95(B13): 21523–21548. doi:10.1029/jb095ib13p21523.

Grosch EG (2018). Metamorphic processes preserved in early Archean supracrustal rocks of the Barberton Greenstone Belt, South Africa. *Geological Society, London, Special Publications* 478(1): 315–334. doi:10.1144/sp478.15.

Halevy I, Bachan A (2018). The geologic history of seawater pH. *Science* 355(6329): 1069–1071. doi:10.1126/science.aal4151.

Hanor JS, Duchač KC (1990). Isovolumetric Silicification of Early Archean Komatiites: Geochemical Mass Balances and Constraints on Origin. *The Journal of Geology* 98(6): 863–877. doi:10.1086/629458.

Hart SR, Staudigel H (1982). The control of alkalies and uranium in seawater by ocean crust alteration. *Earth and Planetary Science Letters* 58(2): 202–212. doi:10.1016/0012-821x(82)90194-7.

Hauff F, Hoernle K, Schmidt A (2003). Sr-Nd-Pb composition of Mesozoic Pacific oceanic crust (Site 1149 and 801, ODP Leg 185): Implications for alteration of ocean crust and the input into the Izu-Bonin-Mariana subduction system. *Geochemistry, Geophysics, Geosystems* 4(8). doi:10.1029/2002gc000421.

Hayashi T, Tanimizu M, Tanaka T (2004). Origin of negative Ce anomalies in Barberton sedimentary rocks, deduced from La–Ce and Sm–Nd isotope systematics. *Precambrian Research* 135(4): 345–357. doi:10.1016/j.precamres.2004.09.004.

Heck PR, Huberty JM, Kita NT, Ushikubo T, Kozdon R, Valley JW (2011). SIMS analyses of silicon and oxygen isotope ratios for quartz from Archean and Paleoproterozoic banded iron formations. *Geochimica et Cosmochimica Acta* 75(20): 5879–5891. doi:10.1016/j.gca.2011.07.023.

Heinrichs T (1984). The Umsoli chert, turbidite testament for a major phreatoplinian event at the onverwacht/fig tree transition (Swaziland supergroup, Archaean, South Africa). *Precambrian Research* 24(3–4): 237–283. doi:10.1016/0301-9268(84)90061-5.

Heubeck C (2019). *The Moodies Group—a High-Resolution Archive of Archaean Surface Processes and Basin-Forming Mechanisms*, p. 133–169. Springer International Publishing. doi:10.1007/978-3-319-78652-0_6.

Heubeck C, Lowe DR (1994). Depositional and tectonic setting of the Archean Moodies Group, Barberton Greenstone Belt, South Africa. *Precambrian Research* 68(3–4): 257–290. doi:10.1016/0301-9268(94)90033-7.

Hofmann A, Bolhar R, Orberger B, Foucher F (2013). Cherts of the Barberton Greenstone Belt, South Africa: Petrology and Trace-Element Geochemistry of 3.5 To 3.3 Ga Old Silicified Volcaniclastic Sediments. *South African Journal of Geology* 116(2): 297–322. doi:10.2113/gssajg.116.2.297.

Hofmann A, Harris C (2008). Silica alteration zones in the Barberton greenstone belt: A window into subseafloor processes 3.5–3.3 Ga ago. *Chemical Geology* 257(3–4): 221–239. doi:10.1016/j.chemgeo.2008.09.015.

Hofmann A, Wilson AH (2007). *Chapter 5.5 Silicified Basalts, Bedded Cherts and Other Sea Floor Alteration Phenomena of the 3.4 Ga Nondweni Greenstone Belt, South Africa*, vol. 15, p. 571–605. Elsevier. doi:10.1016/s0166-2635(07)15055-6.

Hongo Y, Obata H, Sotto Alibo D, Nozaki Y (2006). Spatial variations of rare earth elements in North Pacific surface water. *Journal of Oceanography* 62(4): 441–455. doi:10.1007/s10872-006-0067-1.

Hyslop EV, Valley JW, Johnson CM, Beard BL (2008). The effects of metamorphism on O and Fe isotope compositions in the Biwabik Iron Formation, northern Minnesota. *Contributions to Mineralogy and Petrology* 155(3): 313–328. doi:10.1007/s00410-007-0244-2.

Israel C, Boyet M, Doucelance R, Bonnand P, Frossard P, Auclair D, Bouvier A (2020). Formation of the Ce-Nd mantle array: Crustal extraction vs. recycling by subduction. *Earth and Planetary Science Letters* 530: 115941. doi:10.1016/j.epsl.2019.115941.

Jaffrés JB, Shields GA, Wallmann K (2007). The oxygen isotope evolution of seawater: A critical review of a long-standing controversy and an improved geological water cycle model for the past 3.4 billion years. *Earth-Science Reviews* 83(1–2): 83–122. doi:10.1016/j.earscirev.2007.04.002.

Johnson BW, Wing BA (2020). Limited Archaean continental emergence reflected in an early Archaean ^{18}O-enriched ocean. *Nature Geoscience* 13(3): 243–248. doi:10.1038/s41561-020-0538-9.

Kasting JF, Howard MT, Wallmann K, Veizer J, Shields G, Jaffrés J (2006). Paleoclimates, ocean depth, and the oxygen isotopic composition of seawater. *Earth and Planetary Science Letters* 252(1–2): 82–93. doi:10.1016/j.epsl.2006.09.029.

Kelley KA, Plank T, Ludden J, Staudigel H (2003). Composition of altered oceanic crust at ODP Sites 801 and 1149. *Geochemistry, Geophysics, Geosystems* 4(6). doi:10.1029/2002gc000435.

Kisters AF, Stevens G, Dziggel A, Armstrong RA (2003). Extensional detachment faulting and core-complex formation in the southern Barberton granite–greenstone terrain, South Africa: evidence for a 3.2 Ga orogenic collapse. *Precambrian Research* 127(4): 355–378. doi:10.1016/j.precamres.2003.08.002.

Kitoga L, Zakharov D, Marin-Carbonne J, Boyet M, Moyen JF, Di Rocco T, Pack A, Olivier N, Stevens G (2024). Oxygen and silicon isotopic compositions of Archean silicified lava and cherts of the Onverwacht Group: Implication for seafloor hydrothermalism and the nature of recycled components in the source of granitoids. *Chemical Geology* 670: 122407. doi:10.1016/j.chemgeo.2024.122407.

Kitoga LS, Moyen JF, Boyet M, Marin-Carbonne J, Olivier N, Garçon M, Stevens G (2025). Drone images and geochemical compositions of reference materials and silicified lavas and cherts from the Paleoarchean Barberton Greenstone Belt. OPGC, LMV. doi:10.25519/QXR1-9Y88.

Knauth LP, Lowe DR (1978). Oxygen isotope geochemistry of cherts from the Onverwacht Group (3.4 billion years), Transvaal, South Africa, with implications for secular variations in the isotopic composition of cherts. *Earth and Planetary Science Letters* 41(2): 209–222. doi:10.1016/0012-821x(78)90011-0.

Knauth LP, Lowe DR (2003). High Archean climatic temperature inferred from oxygen isotope geochemistry of cherts in the 3.5 Ga Swaziland Supergroup, South Africa. *Geological Society of America Bulletin* 115: 566–580. doi:10.1130/0016-7606(2003)115<0566:hactif>2.0.co;2.

Konhauser K, Planavsky N, Hardisty D, Robbins L, Warchola T, Haugaard R, Lalonde S, Partin C, Oonk P, Tsikos H, Lyons T, Bekker A, Johnson C (2017). Iron formations: A global record of Neoarchaean to Palaeoproterozoic environmental history. *Earth-Science Reviews* 172: 140–177. doi:10.1016/j.earscirev.2017.06.012.

Krissansen-Totton J, Arney GN, Catling DC (2018). Constraining the climate and ocean pH of the early Earth with a geological carbon cycle model. *Proceedings of the National Academy of Sciences of the United States of America* 115(16): 4105–4110. doi:10.1073/pnas.1721296115.

Kröner A, Anhaeusser C, Hoffmann J, Wong J, Geng H, Hegner E, Xie H, Yang J, Liu D (2016). Chronology of the oldest supracrustal sequences in the Palaeoarchaean Barberton Greenstone Belt, South Africa and Swaziland. *Precambrian Research* 279: 123–143. doi:10.1016/j.precamres.2016.04.007.

Kutyrev A, Bindeman I, O'Neil J, Rizo H (2024). Seawater-oceanic crust interaction constrained by triple oxygen and hydrogen isotopes in rocks from the Saglek-Hebron complex, NE Canada: Implications for moderately low-$\delta^{18}O$ Eoarchean Ocean. *Chemical Geology* 670: 122378. doi:10.1016/j.chemgeo.2024.122378.

Lahaye Y, Arndt N, Byerly G, Chauvel C, Fourcade S, Gruau G (1995). The influence of alteration on the trace-element and Nd isotopic compositions of komatiites. *Chemical Geology* 126(1): 43–64. doi:10.1016/0009-2541(95)00102-1.

Lanari P, Vidal O, De Andrade V, Dubacq B, Lewin E, Grosch EG, Schwartz S (2014). XMapTools: A MATLAB©-based program for electron microprobe X-ray image processing and geothermobarometry. *Computers and Geosciences* 62: 227–240. doi:10.1016/j.cageo.2013.08.010.

Lanier WP, Lowe DR (1982). Sedimentology of the Middle Marker (3.4 Ga), Onverwacht Group, Transvaal, South Africa. *Precambrian Research* 18(3): 237–260. doi:10.1016/0301-9268(82)90012-2.

Ledevin M, Arndt N, Chauvel C, Jaillard E, Simionovici A (2019). The Sedimentary Origin of Black and White Banded Cherts of the Buck Reef, Barberton, South Africa. *Geosciences* 9(10). doi:10.3390/geosciences9100424.

Ledevin M, Arndt N, Davaille A, Ledevin R, Simionovici A (2015). The rheological behaviour of fracture-filling cherts: example of Barite Valley dikes, Barberton Greenstone Belt, South Africa. *Solid Earth* 6(1): 253–269. doi:10.5194/se-6-253-2015.

Ledevin M, Arndt N, Simionovici A, Jaillard E, Ulrich M (2014). Silica precipitation triggered by clastic sedimentation in the Archean: New petrographic evidence from cherts of the Kromberg type section, South Africa. *Precambrian Research* 255: 316–334. doi:10.1016/j.precamres.2014.10.009.

Lei K, Wang H, Wang X, Zhang Q, Li X (2023). Decoupled Zircon Si–O Isotopes Tracing the Supracrustal Silicification and Komatiitic-Derived Fluids in the Source of TTGs. *Geophysical Research Letters* 50(16): 1–9. doi:10.1029/2023gl104002.

Li CF, Li XH, Li QL, Guo JH, Li XH, Yang YH (2012). Rapid and precise determination of Sr and Nd isotopic ratios in geological samples from the same filament loading by thermal ionization mass spectrometry employing a single-step separation scheme. *Analytica Chimica Acta* 727: 54–60. doi:10.1016/j.aca.2012.03.040.

Lowe D, Byerly G (1999). *Geologic evolution of the Barberton Grenstone Belt*. Geological Society of America. doi:10.1130/0-8137-2329-9.

Lowe DR, Byerly GR (1986). Archaean flow-top alteration zones formed initially in a low-temperature sulphate-rich environment. *Nature* 324(6094): 245–248. doi:10.1038/324245a0.

Lowe DR, Byerly GR (2007a). *Chapter 5.3 An Overview of the Geology of the Barberton Greenstone Belt and Vicinity: Implications for Early Crustal Development*, vol. 15, p. 481–526. Elsevier. doi:10.1016/s0166-2635(07)15053-2.

Lowe DR, Byerly GR (2007b). Ironstone bodies of the Barberton greenstone belt, South Africa: Products of a Cenozoic hydrological system, not Archean hydrothermal vents! *Geological Society of America Bulletin* 119(1–2): 65–87. doi:10.1130/b25997.1.

Lowe DR, Byerly GR (2020). The non-glacial and non-cratonic origin of an early Archean felsic volcaniclastic unit, Barberton Greenstone Belt, South Africa. *Precambrian Research* 341: 105647. doi:10.1016/j.precamres.2020.105647.

Lowe DR, Ibarra DE, Drabon N, Chamberlain CP (2020). Constraints on surface temperature 3.4 billion years ago based on triple oxygen isotopes of cherts from the Barberton Greenstone Belt, South Africa, and the problem of sample selection. *American Journal of Science* 320(9): 790–814. doi:10.2475/11.2020.02.

Lécuyer C, Gruau G, Anhaeusser C, Fourcade S (1994). The origin of fluids and the effects of metamorphism on the primary chemical compositions of Barberton komatiites: New evidence from geochemical (REE) and isotopic (Nd, O, H, 30Ar40Ar) data. *Geochimica et Cosmochimica Acta* 58(2): 969–984. doi:10.1016/0016-7037(94)90519-3.

Makishima A, Shimizu H, Masuda A (1986). Precise measurement of cerium and lanthanum isotope ratios. *Journal of the Mass Spectrometry Society of Japan* 35(2): 64–72. doi:10.5702/massspec.35.64.

Marin J, Chaussidon M, Robert F (2010). Microscale oxygen isotope variations in 1.9 Ga Gunflint cherts: Assessments of diagenesis effects and implications for oceanic paleotemperature reconstructions. *Geochimica et Cosmochimica Acta* 74(1): 116–130. doi:10.1016/j.gca.2009.09.016.

Marin-Carbonne J, Chaussidon M, Boiron MC, Robert F (2011). A combined in situ oxygen, silicon isotopic and fluid inclusion study of a chert sample from Onverwacht Group (3.35 Ga, South Africa): New constraints on fluid circulation. *Chemical Geology* 286(3–4): 59–71. doi:10.1016/j.chemgeo.2011.02.025.

Moyen JF, Stevens G, Kisters AF, Belcher RW, Lemirre B (2019). *TTG Plutons of the Barberton Granitoid-Greenstone Terrain, South Africa*, p. 615–653. Elsevier. doi:10.1016/b978-0-444-63901-1.00025-3.

Olivier N, Boyet M (2006). Rare earth and trace elements of microbialites in Upper Jurassic coral- and sponge-microbialite reefs. *Chemical Geology* 230(1–2): 105–123. doi:10.1016/j.chemgeo.2005.12.002.

Paris I, Stanistreet IG, Hughes MJ (1985). Cherts of the Barberton Greenstone Belt Interpreted as Products of Submarine Exhalative Activity. *The Journal of Geology* 93(2): 111–129. doi:10.1086/628935.

Parman SW, Grove TL, Dann JC (2001). The production of Barberton komatiites in an Archean Subduction Zone. *Geophysical Research Letters* 28(13): 2513–2516. doi:10.1029/2000gl012713.

Perry E, Lefticariu L (2007). *Formation and Geochemistry of Precambrian Cherts*, p. 1–21. Elsevier. doi:10.1016/b0-08-043751-6/07138-3.

Pfennig M, Pakulla J, Hasenstab-Dübeler E, Wombacher F, Jodder J, Hofmann A, Münker C (2025). Young oxygenation of the Archean Keonjhar Palaeosol, India, from 138La-138Ce chronometry. *Geochemical Perspectives Letters* 33(51–55): 51–55. doi:10.7185/geochemlet.2503.

Planavsky NJ, McGoldrick P, Scott CT, Li C, Reinhard CT, Kelly AE, Chu X, Bekker A, Love GD, Lyons TW (2011). Widespread iron-rich conditions in the mid-Proterozoic ocean. *Nature* 477(7365): 448–451. doi:10.1038/nature10327.

Planavsky NJ, Robbins LJ, Kamber BS, Schoenberg R (2020). Weathering, alteration and reconstructing Earth's oxygenation. *Interface Focus* 10(4): 20190140. doi:10.1098/rsfs.2019.0140.

Puchtel I, Blichert-Toft J, Touboul M, Walker R, Byerly G, Nisbet E, Anhaeusser C (2013). Insights into early Earth from Barberton komatiites: Evidence from lithophile isotope and trace element systematics. *Geochimica et Cosmochimica Acta* 108: 63–90. doi:10.1016/j.gca.2013.01.016.

Quinn KA, Byrne RH, Schijf J (2006). Sorption of yttrium and rare earth elements by amorphous ferric hydroxide: Influence of solution complexation with carbonate. *Geochimica et Cosmochimica Acta* 70(16): 4151–4165. doi:10.1016/j.gca.2006.06.014.

Reimann S, Heubeck C, Fugmann P, Janse van Rensburg D, Zametzer A, Serre S, Thomsen T (2021). Syndepositional hydrothermalism selectively preserves records of one of the earliest benthic ecosystems, Moodies Group (3.22 Ga), Barberton Greenstone Belt, South Africa. *South African Journal of Geology* 124(1): 253–278. doi:10.25131/sajg.124.0012.

Robert F, Chaussidon M (2006). A palaeotemperature curve for the Precambrian oceans based on silicon isotopes in cherts. *Nature* 443(7114): 969–972. doi:10.1038/nature05239.

Roberts NMW, Santosh M (2018). Capturing the Mesoarchean Emergence of Continental Crust in the Coorg Block, Southern India. *Geophysical Research Letters* 45(15): 7444–7453. doi:10.1029/2018gl078114.

Rollion-Bard C, Marin-Carbonne J (2011). Determination of SIMS matrix effects on oxygen isotopic compositions in carbonates. *Journal of Analytical Atomic Spectrometry* 26(6): 1285–1289. doi:10.1039/c0ja00213e.

Rouchon V, Orberger B (2008). Origin and mechanisms of K–Si-metasomatism of ca. 3.4–3.3 Ga volcaniclastic deposits and implications for Archean seawater evolution: Examples from cherts of Kittys Gap (Pilbara craton, Australia) and Msauli (Barberton Greenstone Belt, South Africa). *Precambrian Research* 165(3–4): 169–189. doi:10.1016/j.precamres.2008.06.003.

Rouchon V, Orberger B, Hofmann A, Pinti DL (2009). Diagenetic Fe-carbonates in Paleoarchean felsic sedimentary rocks (Hooggenoeg Formation, Barberton greenstone belt, South Africa): Implications for CO_2 sequestration and the chemical budget of seawater. *Precambrian Research* 172(3–4): 255–278. doi:10.1016/j.precamres.2009.04.010.

Saitoh M, Olivier N, Garçon M, Boyet M, Thomazo C, Alleon J, Moyen JF, Motto-Ros V, Marin-Carbonne J (2021). Metamorphic origin of anastomosing and wavy laminas overprinting putative microbial deposits from the 3.22 Ga Moodies Group (Barberton Greenstone Belt). *Precambrian Research* 362: 106306. doi:10.1016/j.precamres.2021.106306.

Schmidt K, Bau M, Hein JR, Koschinsky A (2014). Fractionation of the geochemical twins Zr–Hf and Nb–Ta during scavenging from seawater by hydrogenetic ferromanganese crusts. *Geochimica et Cosmochimica Acta* 140: 468–487. doi:10.1016/j.gca.2014.05.036.

Schnabel C, Münker C, Strub E (2017). La–Ce isotope measurements by multicollector-ICPMS. *Journal of Analytical Atomic Spectrometry* 32(12): 2360–2370. doi:10.1039/c7ja00256d.

Schneider K, Hoffmann J, Münker C, Patyniak M, Sprung P, Roerdink D, Garbe-Schönberg D, Kröner A (2019). Petrogenetic evolution of metabasalts and metakomatiites of the lower Onverwacht Group, Barberton Greenstone Belt (South Africa). *Chemical Geology* 511: 152–177. doi:10.1016/j.chemgeo.2019.02.020.

Sharp Z, Kirschner D (1994). Quartz-calcite oxygen isotope thermometry: A calibration based on natural isotopic variations. *Geochimica et Cosmochimica Acta* 58(20): 4491–4501. doi:10.1016/0016-7037(94)90350-6.

Shibuya T, Komiya T, Nakamura K, Takai K, Maruyama S (2010). Highly alkaline, high-temperature hydrothermal fluids in the early Archean ocean. *Precambrian Research* 182(3): 230–238. doi:10.1016/j.precamres.2010.08.011.

Shibuya T, Tahata M, Kitajima K, Ueno Y, Komiya T, Yamamoto S, Igisu M, Terabayashi M, Sawaki Y, Takai K, Yoshida N, Maruyama S (2012). Depth variation of carbon and oxygen isotopes of calcites in Archean altered upperoceanic crust: Implications for the CO_2 flux from ocean to oceanic crust in the Archean. *Earth and Planetary Science Letters* 321–322: 64–73. doi:10.1016/j.epsl.2011.12.034.

Siever R (1992). The silica cycle in the Precambrian. *Geochimica et Cosmochimica Acta* 56(8): 3265–3272. doi:10.1016/0016-7037(92)90303-z.

Śliwiński MG, Kitajima K, Spicuzza MJ, Orland IJ, Ishida A, Fournelle JH, Valley JW (2018). SIMS Bias on Isotope Ratios in Ca-Mg-Fe Carbonates (Part III): $\delta^{18}O$ and $\delta^{13}C$ Matrix Effects Along the Magnesite–Siderite Solid-Solution Series. *Geostandards and Geoanalytical Research* 42(1): 49–76. doi:10.1111/ggr.12194.

Stanistreet IG, de Wit MJ, Fripp REP (1981). Do graded units of accretionary spheroids in the Barberton Greenstone Belt indicate Archaean deep water environment? *Nature* 293: 280–284. doi:10.1038/293280a0.

Stefurak EJ, Fischer WW, Lowe DR (2015). Texture-specific Si isotope variations in Barberton Greenstone Belt cherts record low temperature fractionations in early Archean seawater. *Geochimica et Cosmochimica Acta* 150: 26–52. doi:10.1016/j.gca.2014.11.014.

Stevens G, Moyen JF (2007). *Chapter 5.7 Metamorphism in the Barberton Granite Greenstone Terrain: A Record of Paleoarchean Accretion*, p. 669–698. Elsevier. doi:10.1016/s0166-2635(07)15057-x.

Sugahara H, Sugitani K, Mimura K, Yamashita F, Yamamoto K (2010). A systematic rare-earth elements and yttrium study of Archean cherts at the Mount Goldsworthy greenstone belt in the Pilbara Craton: Implications for the origin of microfossil-bearing black cherts. *Precambrian Research* 177(1–2): 73–87. doi:10.1016/j.precamres.2009.10.005.

Tanner PWG, Miller RG (1980). Geochemical evidence for loss of Na and K from Moinian calc-silicate pods during prograde metamorphism. *Geological Magazine* 117(3): 267–275. doi:10.1017/s001675680003048x.

Tatzel M, Frings P, Oelze M, Herwartz D, Lünsdorf N, Wiedenbeck M (2022). Chert oxygen isotope ratios are driven by Earth's thermal evolution. *Proceedings of the National Academy of Sciences of the United States of America* 120. doi:10.1073/pnas.2213076119.

Tatzel M, Oelze M, Frick DA, Di Rocco T, Liesegang M, Stuff M, Wiedenbeck M (2024). Silicon and oxygen isotope fractionation in a silicified carbonate rock. *Chemical Geology* 658: 122120. doi:10.1016/j.chemgeo.2024.122120.

Taylor S, McLennan S (1985). *The continental crust: its composition and evolution*, p. 301–324. Cambridge University Press. doi:10.1017/cbo9780511575358.014.

Tice MM, Bostick BC, Lowe DR (2004). Thermal history of the 3.5–3.2 Ga Onverwacht and Fig Tree Groups, Barberton greenstone belt, South Africa, inferred by Raman microspectroscopy of carbonaceous material. *Geology* 32(1): 37. doi:10.1130/g19915.1.

Tice MM, Lowe DR (2006). The origin of carbonaceous matter in pre-3.0 Ga greenstone terrains: A review and new evidence from the 3.42 Ga Buck Reef Chert. *Earth Science Reviews* 76(3–4): 259–300. doi:10.1016/j.earscirev.2006.03.003.

Toulkeridis T, Goldstein SL, Clauer N, Kröner A, Todt W, Schidlowski M (1998). Sm–Nd, Rb–Sr and Pb–Pb dating of silicic carbonates from the early Archaean Barberton Greenstone Belt, South Africa: Evidence for post-depositional isotopic resetting at low temperature. *Precambrian Research* 92(2): 129–144. doi:10.1016/s0301-9268(98)00071-0.

Trail D, Boehnke P, Savage PS, Liu MC, Miller ML, Bindeman I (2018). Origin and significance of Si and O isotope heterogeneities in Phanerozoic, Archean, and Hadean zircon. *Proceedings of the National Academy of Sciences of the United States of America* 115(41): 10287–10292. doi:10.1073/pnas.1808335115.

Trower EJ, Lowe DR (2016). Sedimentology of the ∼3.3 Ga upper Mendon Formation, Barberton Greenstone Belt, South Africa. *Precambrian Research* 281: 473–494. doi:10.1016/j.precamres.2016.06.003.

Vezinet A, Pearson D, Thomassot E, Stern R, Sarkar C, Luo Y, Fisher C (2018). Hydrothermally-altered mafic crust as source for early Earth TTG: Pb/Hf/O isotope and trace element evidence in zircon from TTG of the Eoarchean Saglek Block, N. Labrador. *Earth and Planetary Science Letters* 503: 95–107. doi:10.1016/j.epsl.2018.09.015.

Vidal O, Lanari P, Munoz M, Bourdelle F, De Andrade V (2016). Deciphering temperature, pressure and oxygen-activity conditions of chlorite formation. *Clay Minerals* 51(4): 615–633. doi:10.1180/claymin.2016.051.4.06.

Viehmann S, Bau M, Hoffmann JE, Münker C (2018). Decoupled Hf and Nd isotopes in suspended particles and in the dissolved load of Late Archean seawater. *Chemical Geology* 483: 111–118. doi:10.1016/j.chemgeo.2018.01.017.

Viehmann S, Reitner J, Tepe N, Hohl SV, Van Kranendonk M, Hofmann T, Koeberl C, Meister P (2020). Carbonates and cherts as archives of seawater chemistry and habitability on a carbonate platform 3.35 Ga ago: Insights from Sm/Nd dating and trace element analysis from the Strelley Pool Formation, Western Australia. *Precambrian Research* 344: 105742. doi:10.1016/j.precamres.2020.105742.

Villemant B (1988). Trace element evolution in the Phlegrean Fields (Central Italy): fractional crystallization and selective enrichment. *Contributions to Mineralogy and Petrology* 98(2): 169–183. doi:10.1007/bf00402110.

Weis D, Wasserburg G (1987a). Rb-Sr and Sm-Nd isotope geochemistry and chronology of cherts from the Onverwacht Group (3.5 AE), South Africa. *Geochimica et Cosmochimica Acta* 51(4): 973–984. doi:10.1016/0016-7037(87)90109-8.

Weis D, Wasserburg G (1987b). Rb-Sr and Sm-Nd systematics of cherts and other siliceous deposits. *Geochimica et Cosmochimica Acta* 51(4): 959–972. doi:10.1016/0016-7037(87)90108-6.

de Wit MJ, Furnes H (2016). 3.5-Ga hydrothermal fields and diamictites in the Barberton Greenstone Belt—Paleoarchean crust in cold environments. *Science Advances* 2(2): 1–12. doi:10.1126/sciadv.1500368.

Xie X, Byerly GR, Ferrell Jr RE (1997). IIb trioctahedral chlorite from the Barberton greenstone belt: crystal structure and rock composition constraints with implications to geothermometry. *Contributions to Mineralogy and Petrology* 126(3): 275–291. doi:10.1007/s004100050250.

Yoshida S, Ueda H, Asanuma H, Sawaki Y (2024). Y-Ho fractionation during basalt alteration in hydrothermal system: An implication for superchondritic Y/Ho signature recorded in Precambrian banded iron formations. *Chemical Geology* 670: 122421. doi:10.1016/j.chemgeo.2024.122421.

Zakharov DO, Marin-Carbonne J, Alleon J, Bindeman IN (2021). Triple Oxygen Isotope Trend Recorded by Precambrian Cherts: A Perspective from Combined Bulk and in situ Secondary Ion Probe Measurements. *Reviews in Mineralogy and Geochemistry* 86(1): 323–365. doi:10.2138/rmg.2021.86.10.

van Zuilen MA, Chaussidon M, Rollion-Bard C, Marty B (2007). Carbonaceous cherts of the Barberton Greenstone Belt, South Africa: Isotopic, chemical and structural characteristics of individual microstructures. *Geochimica et Cosmochimica Acta* 71(3): 655–669. doi:10.1016/j.gca.2006.09.029.